Ocean Modelling 124 (2018) 75–93

Contents lists available at ScienceDirect

Ocean Modelling

journal homepage: www.elsevier.com/locate/ocemod

Extreme wind-wave modeling and analysis in the south Atlantic ocean

R.M. Campos[a,c,*], J.H.G.M. Alves[b], C. Guedes Soares[a,c], L.G. Guimaraes[c], C.E. Parente[c]

[a] Centre for Marine Technology and Ocean Engineering (CENTEC), Instituto Superior Técnico, Universidade de Lisboa. Rovisco Pais, 1049-001 Lisboa, Portugal
[b] Systems Research Group, Inc., and Environmental Modeling Center, NOAA/NCEP, 5830 University Research Court College Park, Maryland 20740, USA
[c] Programa de Engenharia Oceânica COPPE, Universidade Federal do Rio de Janeiro. Cidade Universitária, Ilha do Fundão, Rio de Janeiro, RJ 21945-970, Brazil

ARTICLE INFO

Keywords:
Extreme winds and waves
Wave hindcasts
Cyclones
South Atlantic ocean

ABSTRACT

A set of wave hindcasts is constructed using two different types of wind calibration, followed by an additional test retuning the input source term S_{in} in the wave model. The goal is to improve the simulation in extreme wave events in the South Atlantic Ocean without compromising average conditions. Wind fields are based on Climate Forecast System Reanalysis (CFSR/NCEP). The first wind calibration applies a simple linear regression model, with coefficients obtained from the comparison of CFSR against buoy data. The second is a method where deficiencies of the CFSR associated with severe sea state events are remedied, whereby "defective" winds are replaced with satellite data within cyclones. A total of six wind datasets forced WAVEWATCH-III and additional three tests with modified S_{in} in WAVEWATCH III lead to a total of nine wave hindcasts that are evaluated against satellite and buoy data for ambient and extreme conditions. The target variable considered is the significant wave height (Hs). The increase of sea-state severity shows a progressive increase of the hindcast underestimation which could be calculated as a function of percentiles. The wind calibration using a linear regression function shows similar results to the adjustments to S_{in} term (increase of β_{max} parameter) in WAVEWATCH-III – it effectively reduces the average bias of Hs but cannot avoid the increase of errors with percentiles. The use of blended scatterometer winds within cyclones could reduce the increasing wave hindcast errors mainly above the 93rd percentile and leads to a better representation of Hs at the peak of the storms. The combination of linear regression calibration of non-cyclonic winds with scatterometer winds within the cyclones generated a wave hindcast with small errors from calm to extreme conditions. This approach led to a reduction of the percentage error of Hs from 14% to less than 8% for extreme waves, while also improving the RMSE.

1. Introduction

Coastal regions in South American countries are widely exposed to extra-tropical and sub-tropical cyclones occurring in the South Atlantic Ocean. Severe winds and waves pose increasing risks to highly populated coastal cities, the fishing industry, harbors and ship routes, and the offshore industry. Therefore, the accurate representation of the wind-waves in the South Atlantic is extremely important for marine safety and offshore industry activities. The goal of this paper it to develop alternative wave hindcasts in the region, discussing different calibration methods, to improve the numerical modeling of significant wave heights (Hs) under extreme conditions. Special attention is devoted to the surface winds, where the Climate Forecast System Reanalysis (CFSR; Saha et al., 2010) is chosen based on selection criteria explained below.

An improved wind database is achieved via the application of two methods of wind calibration using buoy measurements and altimeter data, which are briefly discussed and compared below (details of the methodology are provide in Alves et al., 2017). The skill of the numerical wave model WAVEWATCH III (Tolman et al., 2014) using these wind inputs is assessed, as we also explore the effect of adjusting the wave growth parameters at the input source-term S_{in}, to compose a total of nine wave hindcasts with different wind and wave calibrations. The main goal is to assess and improve the skill of the wave simulations under extreme events, without compromising the average conditions. Moreover, a sensitivity test studies the impact of each calibration on the simulation of significant wave heights, discussing the pros and cons of each database. The South Atlantic Ocean is evaluated as a whole, but the focus is on the south and southeastern coasts of Brazil, where data was more readily available. That region has a wave climate with extreme waves up to 7 m of significant wave height; as studied by Parente (1999), Alves and Melo (2001), Pinho (2003), Pianca et al. (2010), Campos et al. (2012), Nascimento (2013), Godoi et al. (2014), Romeu et al. (2015) and Campos and Guedes Soares (2016a). Moving to

* Corresponding author at: Centre for Marine Technology and Ocean Engineering (CENTEC), Instituto Superior Técnico, Universidade de Lisboa. Rovisco Pais, 1049-001 Lisboa, Portugal.
E-mail address: ricardo.campos@noaa.gov (R.M. Campos).

https://doi.org/10.1016/j.ocemod.2018.02.002
Received 9 August 2017; Received in revised form 15 January 2018; Accepted 1 February 2018
Available online 03 February 2018
1463-5003/

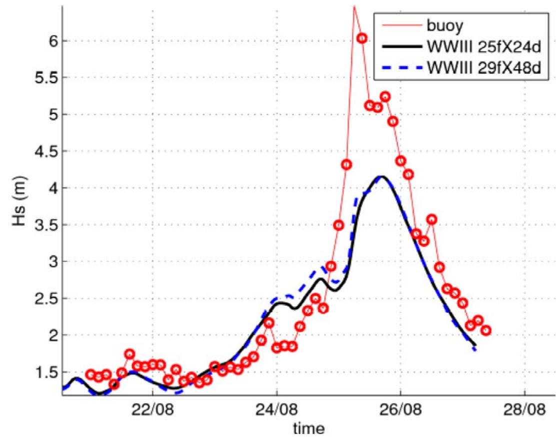

Fig. 1. Extreme event occurred in August 1992 measured by a heave-pitch-roll buoy at 22.31°S / 39.58°W moored in deep water (1250 m). Red: Significant wave height in meters measured by the buoy. Solid black: WAVEWATCH III simulation using spectral discretization of 25 frequencies and 24 directions, and grid resolution of 0.3° Dashed blue: WAVEWATCH III simulation using spectral discretization of 29 frequencies and 48 directions, and grid resolution of 4′ (0.067°). (For interpretation of the references to colour in this figure legend, the reader is referred to the web version of this article.)

southern regions, Dragani et al. (2013) and Alonso et al. (2015) discuss in details the synoptic patterns associated with the highest waves at the mouth of Rio de la Plata. Vanem and Walker (2013) consider the significant wave height as the most important parameter in terms of environmental threat to ship and marine structures, as it represents the total energy of the power spectrum. Therefore, the significant wave height (Hs) is the target variable studied in this paper.

In order to improve the information about the metocean climate and extreme events in Campos Basin (offshore Rio de Janeiro, Brazil), in 1991 a heave-pitch-roll wave buoy was moored at 22.31°S / 39.58°W in water depth of 1250 m, which measured winds and waves for approximately three years. The most extreme event registered by this dataset is presented in Fig. 1, on 25 August 1992, when the significant wave height reached 6.5 m. It became a benchmark in terms of extreme event in southeast Brazil. One of the first wave simulations using WAVEWATCH III wave model forced with Climate Forecast System Reanalysis (CFSR, Saha et al., 2010) for that area led to the black solid line of Fig. 1. The wave simulation used the CFSR wind resolution, approximately 0.3° and 1 h, within a global grid. The source term applied in WAVEWATCH III version 3.14 was ST2 (Tolman and Chalikov, 1996) and the directional spectrum matrix contained 25 frequencies and 24 direction. As shown in Fig. 1, the model result significantly underestimates the measurements, to an extend that an important discussion about the accuracy of hindcasts in the location emerged, together with a great concern about their use for decisions involving marine safety.

The low accuracy of wave simulations under extreme conditions has been widely discussed (e.g. Cardone et al., 1996; Swail and Cox, 2000; Stopa and Cheung, 2014; Campos and Guedes Soares, 2016b etc) and the proper investigation of the uncertainties sources becomes crucial for the improvement of the wave simulation (Cavaleri et al., 2007; Rogers et al., 2012a). Rogers et al. (2012a) describe three categories of error sources: numerics and resolution, physics, and forcing. The forcing wind is pointed to be an important source since the wave simulations are very sensitive to input wind fields, as demonstrated by Teixeira et al. (1995), Holthuijsen et al. (1996), Ponce de Leon and Guedes Soares (2008), Van Vledder and Akpinar (2015) and Campos et al. (2016c), especially due to the quadratic dependence of the significant wave height related to the surface wind speed. Cavaleri (2009) states that, although the great improvement in wave modeling with respect to the past, the wind accuracy is still a relevant factor at the peak of the storms.

This was the main motivation for the wind calibrations and the construction of six wind input databases in the present study. Moreover, the wave model physics and source terms parameterization also have a great impact on the accuracy of the wave simulations, as explained by many authors such as Janssen (1982), Burgers and Makin (1992), Tolman and Chalikov (1996), Ardhuin et al. (2007a), Babanin et al. (2007), Rogers et al. (2012b), Ardhuin et al. (2010) and Alves et al. (2014). It has been taken into account in the present during the set-up of the wave simulation, choosing the proper source terms and parameterizations. Additional discussions about wave modeling accuracy can be found in Padilla-Hernandez et al. (2004), Cavaleri and Bertotti (2004), Caires et al. (2004), Feng et al. (2006), Ardhuin et al., (2007b), Appendini et al. (2012), Chawla et al. (2013) and, concerning specifically extreme waves associated with cyclones, in Rocha et al., (2004), Tolman and Alves (2005), Cardone and Cox (2011), Ponce de Leon and Guedes Soares (2014) and Alves et al. (2015). A good illustration of extreme waves in the South Atlantic is provided by Innocentini and Caetano Neto (1996), who performed a case study of the 9th August 1988 South Atlantic storm, when the Brazilian news media reported the loss of at least one life, waves of 3 m and higher, and the disappearance of a drainage pipe, which weighed 8000 kg, off the shores of Rio de Janeiro. A more recent study of Innocentini et al. (2014) used CFSR winds forcing WAVEWATCH III to produce a 31-yr wave hindcast in the South Atlantic Ocean. They suggested a new procedure to deal with potentially dangerous swells, developed to detect distantly generated systems reaching the Brazilian coast.

Another challenge to produce useful simulations of extremes in the South Atlantic is the difficulty of producing accurate simulations in a region with very sparse data and few in situ measurements, especially because extreme events depend on the position of large fetches and cyclone tracks, as discussed by Campos et al. (2012). Gan and Rao (1991), Sugahara (2000), Reboita (2008) and Reboita et al. (2009) described the main cyclonegetic areas in the Southwest Atlantic Ocean. Considering the large fetches involved with wave generation in the area under investigation and the poor coverage by in situ platforms, the use of satellites became an important source of data in the present study. The amount of scatterometer data has significantly increased since the early 2000′s, especially with QuikSCAT (JPL, 2001), which composed the main source of satellite data in this work. Due to QuikSCAT gaps in between satellite swaths, the use of more remotely-sensed observations became necessary to properly cover the cyclone propagation. This problem could be solved with the blended surface wind databases of SeaWinds (NCDC/NOAA; Zhang et al., 2006), which is used in association with QuikSCAT data in the present study to evaluate and calibrate the CFSR reanalysis, within a domain ranging from 70°S to 5°S and 70°W to 0° Despite the heavy dependence on remotely-sensed data, some buoys were also used to provide "ground truth" in this study, illustrated in Fig. 2. No shallow water buoys are included so this work is restricted to deep water and large scale analyses. Considering the availability of buoy and satellite data, the period for wind calibration and wave hindcasting extended from 2002 till 2009. Wave hindcasts are evaluated using buoys and altimeter data. As the spatial distribution of wave hindcast errors is an important discussion in the present paper, which is only possible with assessments against altimeter data, the analysis of the wave period is not included, since altimeter databases do not provide this parameter.

Section 2 is dedicated to the wind analyses. Sections 2.1 and 2.2 evaluate the 10-meter winds of CFSR against metocean buoys and scatterometer data. Section 2.3 describes the cyclone identification followed by the construction of composites of extreme events, where the spatial distribution of wind errors is highlighted. Section 2.4 presents the wind calibration using buoy and scatterometer data. Section 3 is dedicated to the wave simulations, where wave hindcasts are constructed testing different parameters and then evaluated against buoy and altimeter data, considering calm and extreme conditions. Finally,

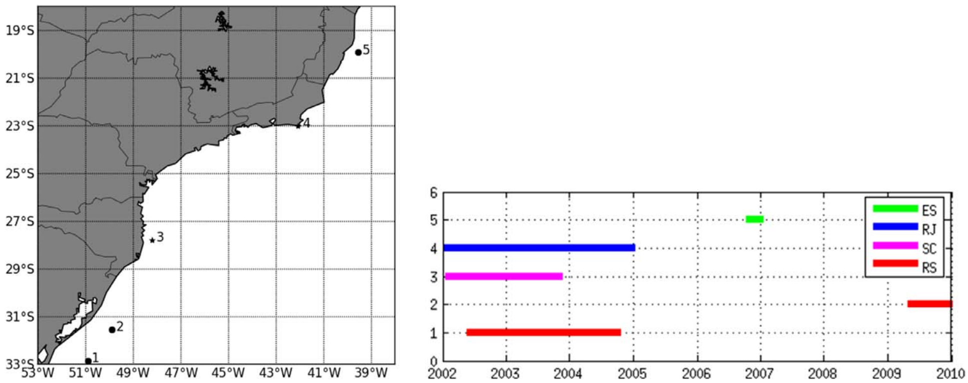

Fig. 2. Buoys location on the left and duration of available buoy measurements on the right, related to each buoy (y-axis). RS: Rio Grande do Sul, SC: Santa Catarina, RJ: Rio de Janeiro and ES: Espirito Santo. Buoys (1), (2) and (5) provided meteorological measures. Water depths (meters) and distance from the coast (kilometers) of buoys 1 to 5 are respectively: (85 / 135), (230 / 101), (90 / 30), (100 / 5) and (800 / 46).

Section 4 has the final discussion and conclusions.

2. Assessment and calibration of CFSR surface winds

NCEP and the European Center for Medium-Range Weather Forecast (ECMWF) have been producing state-of-the-art reanalysis products for the last three decades (Kalnay et al., 1996; Kistler et al., 2001; Gibson et al., 1997; Uppala et al., 2005; Dee et al., 2011). The most recent NCEP reanalysis database was generated as part of the Climate Forecast System Reanalysis project (CFSR, Saha et al, 2000). The CFSR reanalysis is a global product covering the period 1979 to 2009 in its first release. The wind fields have resolution of 18.5′ ($\sim 0.31°$) and 1 h The CFSR reanalysis uses the NCEP atmospheric Global Forecast System (GFS) with a robust data assimilation system. A detailed description is provided in Saha et al. (2010). QuikSCAT scatterometer wind is one among several sources of measurements assimilated by CFSR. However, the optimization in the assimilation process takes into account the whole atmospheric model, with several layers, and the stability of the solution. Therefore, the CFSR 10-m wind, the main parameter for wave simulations, can diverge to the scatterometer winds under certain conditions.

Stopa and Cheung (2014) evaluated the flagship reanalyses from NCEP and ECMWF, CFSR and ERA-Interim, respectively. They found important divergences between both NCEP and ECMWF reanalyses for the higher wind percentiles, mainly for the top 1% level. The authors conclude that both reanalyses underestimate extreme events above the 95% percentile. According to their results, ECMWF's ERA-Interim underestimates the upper percentile measurements by 8% on average, whereas NCEP's CFSR shows better agreement with observations, with an underestimation of 3% on average. This better agreement between CFSR and observed upper percentiles extends to the 99.8% mark, when the quality deteriorates significantly. Result of Stopa and Cheung (2014) were later confirmed by Campos and Guedes Soares (2016b) with an evaluation of CFSR and ERA-Interim using GlobWave satellite data. Among available surface winds from global reanalyses, the CFSR was selected for our study because of the availability of public data at higher spatial and temporal resolutions, and for its better performance at higher wind speed percentiles. The reasoning may be summarized as follows:

1. Higher resolution: the focus of this paper is on extreme events and the spatial and temporal resolution is of great importance for the proper simulation of cyclones and extreme waves, as discussed by Cavaleri and Bertotti (2004), Cavaleri and Bertotti (2006) and Cavaleri et al. (2007).
2. Performance of the higher percentiles, as described by Stopa and Cheung (2014).
3. Portability for operational applications: CFSR was produced with the GFS model, which is also used operationally at NCEP. Therefore, the methodology applied in the present study using a NCEP hindcast can be adopted and implemented for NCEP forecasts.
4. Both CFSR and the operational GFS provide publicly available datasets, which favor usage and replication of the results reported presently by the public.

Below a general description of the methodologies for obtaining forcing wind databases that could be used to improve estimates of extreme waves in the South Atlantic is provided. A more detailed description of the approaches and methodologies is also found in Alves et al. (2017).

2.1. Evaluation of CFSR wind speeds relative to buoys

The location and duration of buoys used in the present paper is presented by Fig. 2. All buoys provide wave measurements but only buoys (1), (2) and (5) carried meteorological instruments to provide wind data. The platform with the longest duration and strategic position at the most southerly location is buoy 1 (S Rio Grande do Sul, at 32.86°S / 50.89°W) moored at 85-m water depth from 05/2002 to 10/2004. Therefore, it will be the main source of observation to evaluate and calibrate CFSR winds. Winds were converted to the CFSR wind speed height of 10 m using the LKB method (Liu, Katsaros & Businger) described by Liu et al. (1979). Validation statistics used henceforth for wind and wave parameters are: mean error (ME, measurement minus reanalysis), correlation coefficient (CC), scatter index (SI) and root mean square error (RMSE):

$$ME = \frac{\sum_{i=1}^{n} (S_i - R_i)}{n} \tag{1}$$

$$RMSE = \sqrt{\frac{\sum_{i=1}^{n} (S_i - R_i)^2}{n}} \tag{2}$$

$$SI = \frac{RMSE}{\bar{S}} \tag{3}$$

$$CC = \frac{\sum_{i=1}^{n} (S_i - \bar{S})(R_i - \bar{R})}{\left(\sum_{i=1}^{n} (S_i - \bar{S})^2 \sum_{i=1}^{n} (R_i - \bar{R})^2\right)^{1/2}} \tag{4}$$

where S are the observations (buoy or satellite measurements), R are the reanalysis values, the over bar indicate mean values through time and n denotes the number of data pairs. Positive values of ME (bias) indicate underestimation of the model relative to observations, while negative values of ME indicate overestimation. Since the main focus in the present study is on extreme events, the same metrics were also calculated for the values above the 95% and 99% percentiles. Finally, the ratio between the CFSR quantile divided by the buoy quantile were also computed, for the same levels of 95% and 99%, which means the inverse of the Cumulative Distribution Function (CDF) of the reanalysis related to the buoy. When ratio is above 1.0, the wind speed of CFSR is greater than the buoy and when it is below 1.0 the wind speed of the buoy is greater than CFSR. Table 1 presents results for the bulk of data,

Table 1
Results of evaluation of CFSR compared to three offshore buoys in Brazil, for wind speed at 10-meters. The notation .p95 and .p99 indicate that the error metrics are applied to values above the 95% and 99% percentile levels. CC: correlation coefficient. ME: mean error. RMSE: root mean square error. SI: scatter index.

buoy	CC	ME	RMSE	SI
1	0.85	−0.08	1.47	0.45
2	0.85	1.17	1.76	0.23
5	0.67	1.93	2.22	0.30

buoy	ME.p95	RMSE.p95	Si.p95	ME.p99	RMSE.p99	Si.p99	$\frac{QU_{p95}^{CFSR}}{QU_{p95}^{buoy}}$	$\frac{QU_{p99}^{CFSR}}{QU_{p99}^{buoy}}$
1	0.51	2.58	0.15	0.66	1.67	0.08	0.95	0.96
2	1.14	3.36	0.18	1.06	2.09	0.10	0.91	0.94
5	−0.48	0.99	0.08	−0.88	1.60	0.12	0.82	0.96

and also restricted to extreme events. Before making assertions on the quality of CFSR winds relative to available buoy data, two limitations must be considered. First, the short measurements duration at buoys 2 and 5 cast doubts on the reliability and statistical significance of their data. Second, even considering the longer buoy 1 dataset, measured 95% and 99% percentiles had most intense winds at 14 and 17 m/s, respectively, which also cast doubts to their being representative of "true" extreme conditions. Therefore, the term "extreme" referring to upper percentiles in Table 1 indicate wind intensities above 14 m/s – which for several locations with severe wind climate it would not be considered extreme.

Table 1 shows a relative good agreement between CFSR and buoy data, with CC around 0.8 and small ME and RMSE. Moving to the upper percentile of 95%, the ME increases at buoy 1 and CFSR starts to underestimate the events. ME values increase even more at the percentile of 99%. The ME and RMSE become higher under extreme conditions, whereas SI are reduced. Therefore, the reanalysis does not necessarily deteriorate moving to extreme events; the precision showed small changes and the accuracy indicated an increasing reanalysis underestimation at buoy 1 with intensity. An alternative way to analyze the performance of the reanalysis with the intensity is by looking at the scatter plots, QQ-plots and probability distributions, shown in Fig. 3. The scatter plots indicate a large spread of co-located CFSR and buoy data. The QQ-plots indicate a good representation of CFSR winds for wind intensities up to 10 m/s. From that point, CFSR consistently underestimates higher wind speeds. The probability density functions show that the shape of the functions diverges, mainly in terms of kurtosis, which impacts long-term distribution fits and extrapolations. Although the CFSR evaluation using buoy data is a relevant first step to qualify the reanalysis, the available buoy dataset is not sufficient for a proper statistical analysis, regarding both temporal and spatial coverage. Therefore, in the next item, the use of satellite data will make possible the evaluation of the cyclonic winds and fetches that generate the most extreme waves during the period from 2002 to 2009.

2.2. Evaluation of CFSR relative to scatterometer winds

In this section, surface wind speeds from CFSR are compared to measurements made by QuikSCAT during severe weather events associated with extreme significant wave heights in the western South Atlantic. Comparisons are made using a grid with a resolution of 0.25° X 0.25° and preserve the time of QuikSCAT tracks, whereby CFSR data is interpolated in space and time to match measurements. Wave buoy measurements were used to select the periods when extreme wave heights occurred, including a lead up time of 72 h before the observed time of maximum wave height. The use of QuikSCAT data under extreme wind conditions above 20 m/s might be considered questionable, since the scatterometer has increasing uncertainties for high intensity storms with heavy clouds (Freilich and Vanhoff, 2006; Quilfen et al., 2007). However, Quilfen et al. (2007), after performing a complete evaluation of QuikSCAT data, found that wind vector retrieval under extreme condition is feasible. Besides, the conditions considered "extremes" in extra-tropical cyclones in the southwest Atlantic are much less intense than those associated with tropical cyclones in the Northern Hemisphere.

The nine most severe events were selected from the buoy measurements, all of them associated with peak wave periods from 11 to 15 seconds, and directions from southeast to southwest. Most part of the events occurred during winter and fall. Synoptic conditions reveal cold fronts with strong southerly winds hitting the southeast coast of Brazil before the maximum of wave heights. The cyclones quickly propagate towards east and southeast, creating a large fetch that dominated the left part of the cyclone. The first line of Fig. 4 illustrates this evolution, with relatively short-to-medium fetch with intense winds of 25 m/s on the July 29. As the cyclone evolved, a larger fetch developed on July 30, with lighter winds of 15 m/s. The second line of Fig. 4 presents the difference between QuikSCAT and CFSR surface winds. Hot colors indicate underestimation of CFSR, while cold colors indicate overestimation. Although CFSR reanalysis assimilated QuikSCAT from 2001 to 2009, the evolution of the cyclone shows that CFSR consistently underestimates measurements within the cyclone, especially at the left part of the low pressure system associated with southerly winds. Differences are around 5 m/s in a relatively small area with strong winds, and from 2 to 3 m/s over the larger fetch. This represents an underestimation of 10% to 25%, in areas where QuikSCAT is more intense than CFSR. The same differences with common pattern were found in other extreme events. Considering that the atmospheric conditions in the South Atlantic Ocean associated with the most extreme Hs events are reasonably similar, and the analysis and inclusion of many figures would make this paper unnecessary long, it was decided to present a composition of all extreme events in terms of the average surface winds before the peak of the wave measurement. We call these images "composites", presented in the next section, and they indicate where the regions containing the most differences between CFSR and QuikSCAT occur, as well as the time evolution of the CFSR underestimation areas.

2.3. Cyclone identification and composites of extreme winds

Prior to building composites, a cyclone tracker based on Murray and Simmonds (1991), Sugahara (2000), Reboita (2008) and Reboita et al., (2009) was implemented to identify the center of cyclones and to calculate maximum and average parameters of atmospheric variables within storms. In order to enhance vortices and events with strong vorticity, the method of Kurihara et al. (1993) was applied, which facilitated the identification. The SeaWinds and CFSR databases were used for the cyclone tracking, and results were combined to create a database including latitudes, longitudes, dates, minimum, maximum and mean wind intensities, vorticities and pressures for each cyclone. Occurrences of cyclones show a high density at 35°S, close to Uruguai and Rio Grande do Sul (Brazil), and the greatest intensities are found below 40°S. Campos et al. (2012) discuss this balance between positioning and intensity associated with the severity of extreme events in terms of Hs in Brazil. The cyclone identification was applied to

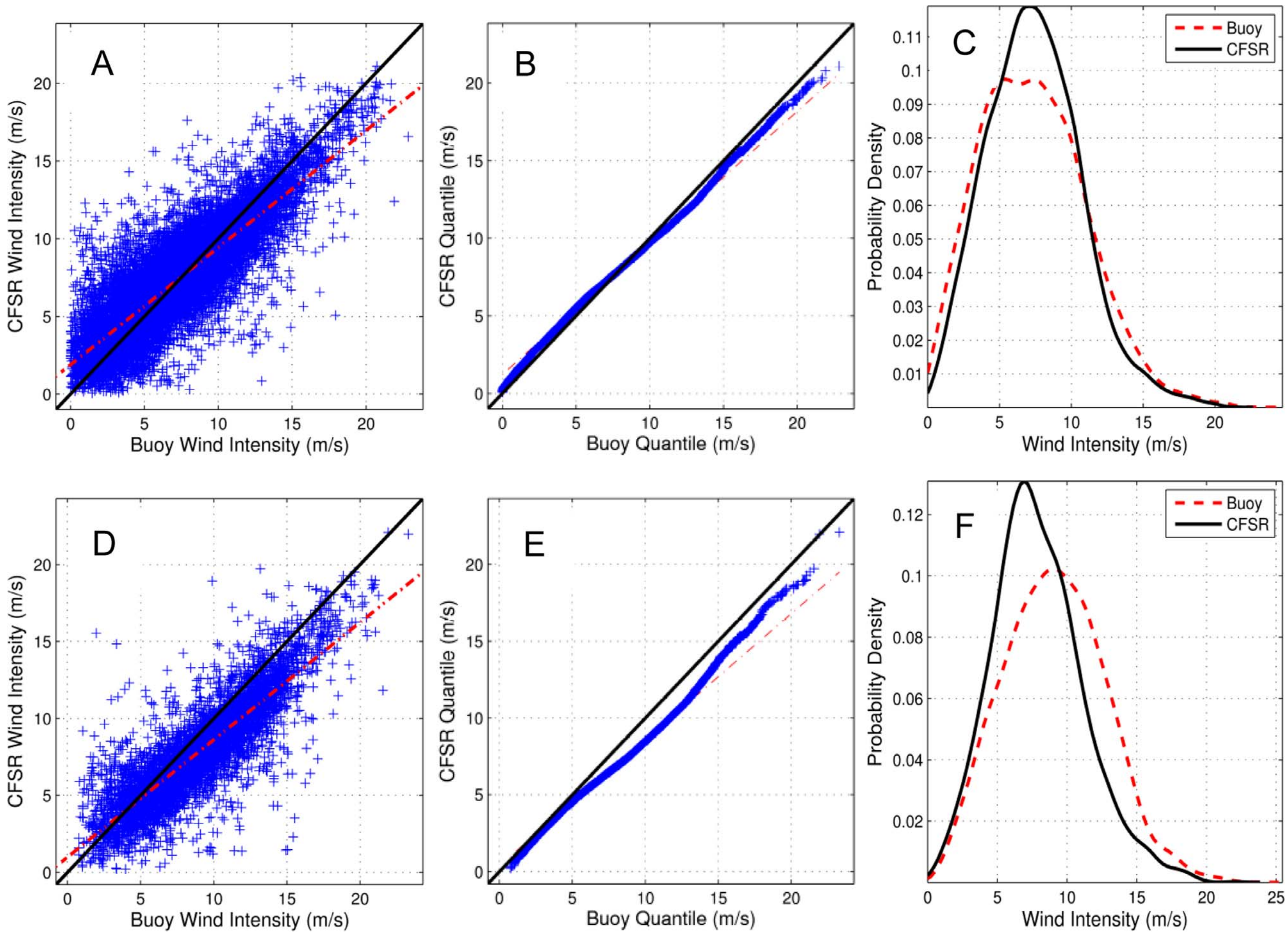

Fig. 3. Scatter plots (on the left; A, D), QQ-Plots (center; B, E) and Probability Density Functions (on the right; C, F) comparing the CFSR wind intensities (y-axis) with buoy wind intensities (x-axis). The first line (A, B and C) represents buoy 1 while second line (D, E and F) represents buoy 2.

considered period from 2002 to 2009, including the 47 most extreme events selected on the basis of buoy data. Table 2 shows the results. The number of selected events is related to the top 1% independent events measured by the wave buoys - in all cases generated by cyclones. In terms of cyclogenesis and positioning, the latitude is around 40°S, with tracks moving towards southeast. The mean sea level pressure (MSLP) has the lowest values at 48 h and 6 h, while the average wind speed has highest values 48 h before the peak of the wave measurements. Maximum winds within cyclones are most intense 12 h before peak measured waves.

Fig. 5 summarizes the error of composites of CFSR surface wind speeds relative to measurements, for up to three days before the peak of Hs. The spatial distribution clearly shows some important characteristics governing the occurrence of extremes, with bias distribution being consistent with the changes in the wind fields. Average wind intensity and direction confirm the well-known persistence of southwesterly winds in southern Brazil, Uruguay and northeast Argentina. The strongest winds are found again 48 h before maximum waves are observed. Even rows of panels in Fig. 5 (lines 2 and 4) present the differences in wind intensity QuikSCAT minus CFSR. Once again, hot colors indicate CFSR underestimation, while cold colors indicate overestimation. Maps confirm that CFSR generally underestimates intensities in the area of maximum winds, mainly associated with southerly directions. The average underestimation varies from 1 m/s to 2 m/s, especially in the western part of the Atlantic Ocean. The evolution in time indicates a displacement of the CFSR underestimation area, following cold fronts coupled with the tracked cyclones. Underestimation becomes more significant 48 h prior to maximum waves, mostly at southern latitudes. Around 24 h prior to maximum waves, the largest underestimation (red shaded areas) shifts northward, nearing southeastern Brazil and 20°S. In the 12 h lead to maximum measured waves, the underestimation persists with more or less the same spatial extent, having a small spread towards eastern longitudes. As the surface winds are the most important variable for the numerical wave forecasts, Fig. 5 maps regions that must be carefully investigated as potential sources of largest inaccuracies in winds used for simulating extreme waves in the south and southeast of Brazil.

2.4. Improved winds for extreme wave simulations

It was shown that CFSR surface winds are generally skillful for ambient conditions, but consistently underestimate the highest observed wind percentiles, when both buoys and, particularly, scatterometer data are considered. When compared to QuikSCAT, CFSR showed large errors around 5 m/s within the cyclones with wind intensities up to 35 m/s. These inaccuracies at strong wind speeds are crucial for extreme wave simulation. Therefore, an adjustment method was investigated to improve CFSR higher-percentile winds in the South Atlantic Ocean. In view of the availability of measurements with different characteristics used for the CFSR assessment, we performed a series of alternative calibration approaches as follows. First, a very simple univariate linear regression model is applied using buoy measurements only – a quick and widely-used solution in the private consultancy industry. Thereafter, more complex methods using satellite measurements, merged with the CFSR reanalysis within the area of influence of cyclones are applied. The ultimate objective of the calibration performed below is the generation of a consistent, high-quality surface wind database, optimally adjusted to force a wave model in a

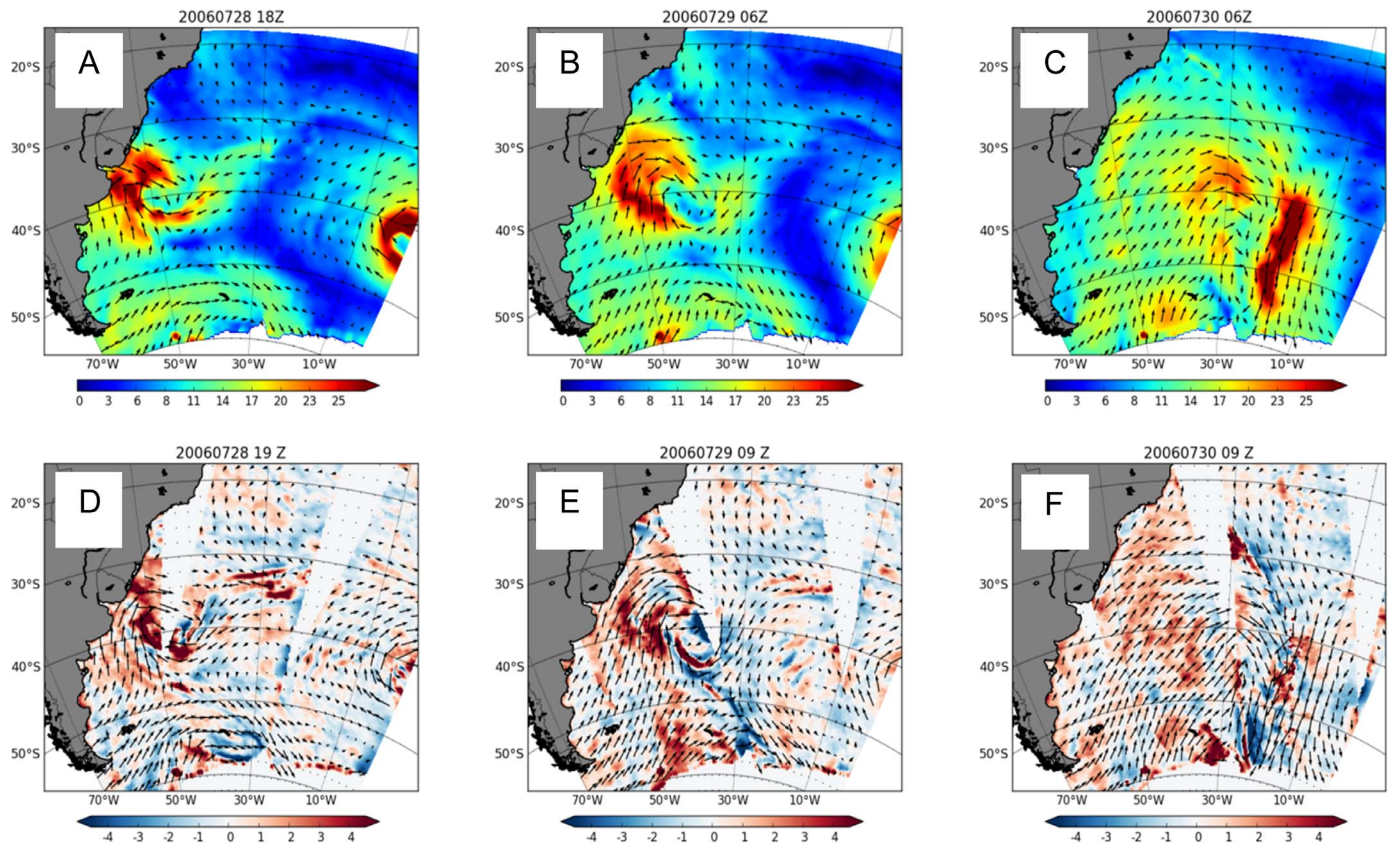

Fig. 4. Surface winds in the South Atlantic Ocean, synoptic evolution that generated the most extreme waves recorded in Brazil, in July of 2006. First line (A, B and C): SeaWinds 10-meter winds (m/s). Second line (D, E and F): QuikSCAT winds minus CFSR winds (m/s).

Table 2
Average position and variables of the cyclones associated with the 47 extreme events of wave heights measured by metocean buoys in Brazil. The average is calculated for each instant before the maximum wave measured, from 00 hours to 72 h before. MSLP: Mean Sea Level Pressure (hPa). U_{10m}: 10-meters wind intensity.

Hours before events	Lat	Lon	MSLP (hPa)	$\overline{U_{10m}}$	U_{10m}^{max}
00	−39.03	−38.47	961.9	12.10	28.52
06	−39.53	−37.09	958.6	12.02	27.70
12	−39.46	−38.44	961.8	11.83	31.36
24	−40.80	−38.05	962.8	12.53	29.29
48	−41.22	−41.62	949.4	13.81	30.04
72	−41.32	−41.28	964.6	11.94	31.30

way that both ambient and extreme waves are skillfully simulated.

2.4.1. Linear regression model

The use of a linear regression model is a common approach to calibrate wind intensity and wave height in several applications, using observations or numerical prediction models. Tolman (1998), Alves et al. (2009) and Caires and Sterl (2005) are examples of simple wind and wave calibrations using linear regression, and composed the methodology applied in this section. Pairs of wind data were built from CFSR and buoys, which were used to calculate quantiles ranging from 1% to 100%. Results were plotted as illustrated in Fig. 6 (black dots). Two linear regression fits were calculated: one for the whole set of quantiles (grey line), and another for the values above the 80th percentile (red line), approximately above 10 m/s. Eqs. 5 and 6 are the resulting linear regression models adjusted to the bulk percentiles, and to the upper percentiles only, respectively.

$$U_{10m}^{Buoy} = (1.094{*}U_{10m}^{CFSR}) - 0.370 \tag{5}$$

$$U_{10m}^{Buoy} = (1.049{*}U_{10m}^{CFSR}) - 0.140 \tag{6}$$

A first candidate wind database for application to simulation of wave extremes was built applying Eq. (6) to the CFSR winds in the South Atlantic Ocean (CFSR.LR). Only the wind intensity is modified. Changes obtained with this approach represent an increase of 5% to 6% of the CFSR wind intensity within more severe storm systems observed in the South Atlantic. This calibration was not meant to be a reliable optimized solution, since such regression model is oversimplified and does not take into account the spatial variation of CFSR error. Instead, it is applied to evaluate the impact of a quick and simple calibration compared to other methods later discussed in this paper.

2.4.2. Cyclonic wind replacement and blending

The evaluation of CFSR surface winds indicates that it severely underestimates upper-percentile winds within cyclones in the South Atlantic, which cannot be corrected using a simple linear regression model. Chawla et al. (2013) also reported problems in the NOAA´s wave hindcast using WAVEWATCH III associated with CFSR in the Southern Hemisphere. Furthermore, the most critical regions in terms of CFSR wind speed underestimation, the cyclonic areas, rarely pass through the buoy´s position. An original method devised as part of the present study is proposed where the perceived deficiencies of the CFSR cyclonic winds are remedied, whereby “defective” wind fields are replaced with data measured by satellites, and the consistency of overall fields ensured by a blending algorithm. Replacement and blending are performed following the center of cyclones. The basis of the proposed approach follows three steps. First, cyclones are identified using the cyclone tracking algorithm previously explained. Second, cyclonic wind fields are isolated from the background/ambient wind signal following the approach of Kurihara et al. (1993). Finally, new cyclonic winds are added to the background field, following the approach of

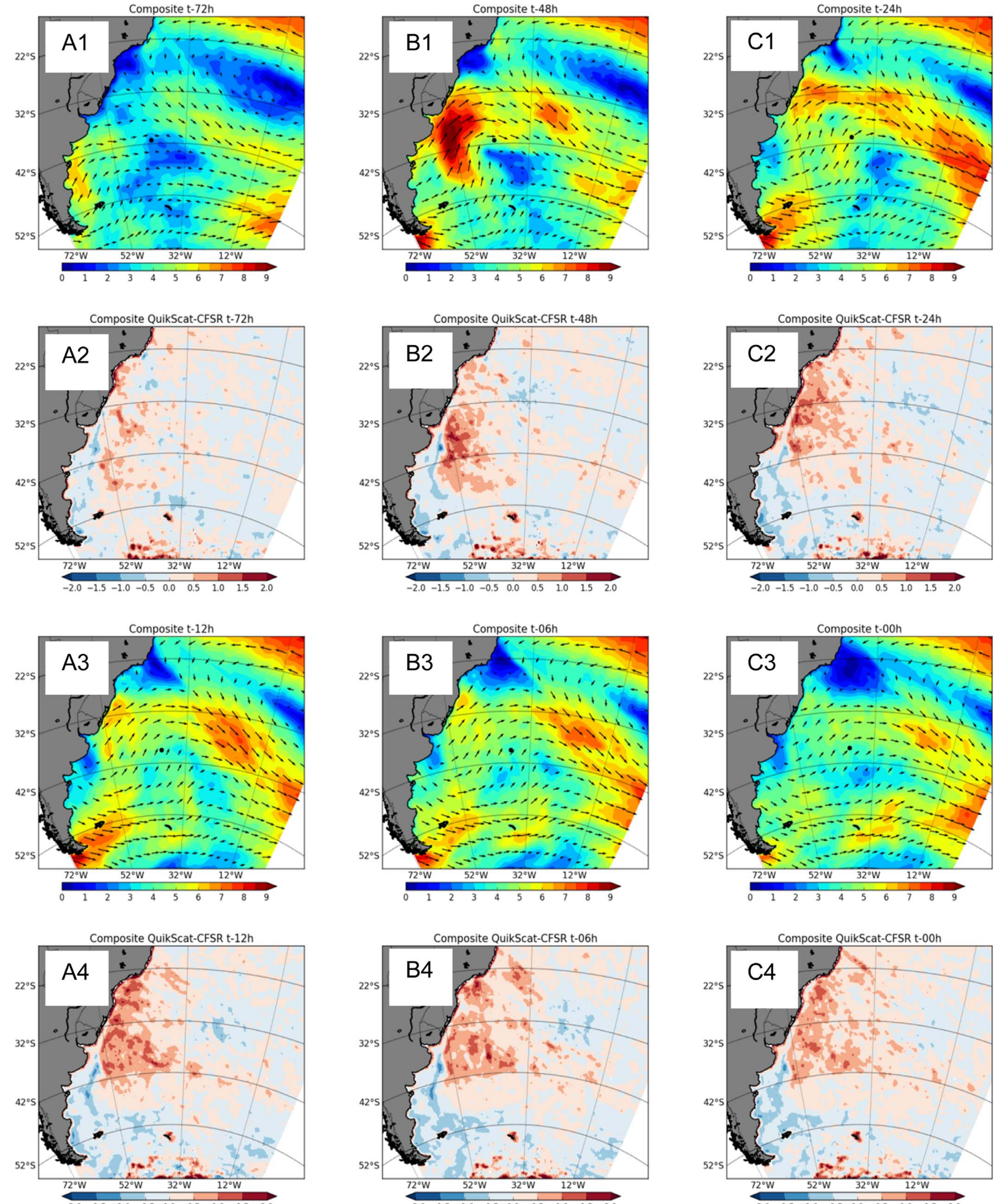

Fig. 5. Composites of wind intensity (first and third lines, m/s) and wind intensity difference of QuikSCAT minus CFSR (second and fourth lines, m/s). Average at each hour before the maximum wave measured in Brazil, from 00 hours to 72 h before.

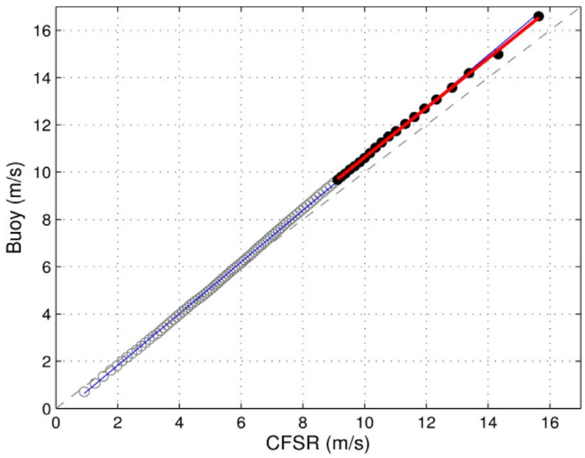

Fig. 6. Buoy quantiles versus CFSR quantiles for 10-meters wind intensity. Grey line shows a linear regression fit considering all quantiles while the red line shows the fit to quantiles above the percentile of 80% (approximately 10 m/s). (For interpretation of the references to colour in this figure legend, the reader is referred to the web version of this article.)

Chao et al. (2005). A key step is to separate cyclonic winds from the background, ambient fields, and extract them for replacement. Kurihara et al. (1993) use iterative filters to remove high frequency disturbances from the large-scale wind fields so that a smooth environmental field is produced. The latter is retained, and provides the ambient component of the new surface wind field database. Due to the gaps between QuikSCAT swaths, the SeaWinds database was used in combination with it, allowing the reconstruction of surface winds from each cyclonic event in a more reliable way.

SeaWinds is a 6-hourly satellite database, which was interpolated onto the 1-hourly sampling, same as CFSR, using the technique of Tolman and Alves (2005) instead of the traditional bi-linear interpolation that deteriorates the structure of small cyclones with fast propagation ("German-salsa" effect). Therefore, an algorithm was developed to separate the cyclonic and background winds from the SeaWinds database, following again the approach of Kurihara et al. (1993), and to perform separately background and storm-centered interpolation between consecutive SeaWinds time slices, providing hourly wind fields, which are then recombined onto a consistent hourly SeaWinds database. Fig. 7 exemplifies the process for two cyclones in July 2007, associated with an extreme event with Hs of 6.1 m measured in the southeast of Brazil.

The blending of CFSR ambient fields with satellite-based cyclonic wind fields generated two distinct surface wind databases, which differ only in terms of the CFSR ambient winds. In the first set no calibration is applied to CFSR ambient conditions, while in the second set the linear regression is used to calibrate the CFSR ambient winds. Both have satellite data of SeaWinds and QuikSCAT within cyclones using the same methodology. Results are presented in Fig. 8 for an event in June 2008, when a cyclone generated the highest wave measured in Brazil, with 7.6 m of Hs. Fig. 8C illustrates the differences of wind intensities from the new database minus the original CFSR - in red are regions where satellite winds are more intense than CFSR. It shows that QuikSCAT data represent more accurately sharp fronts and higher wind speeds in intense cyclones. Therefore, QuikSCAT winds provided an alternative framework for improving the simulation of extreme waves, in combination with SeaWinds. Stencils on Fig. 8D depict the areas where each different wind source was retained, as well as transition zones. Areas with heavy clouds where QuikSCAT flags pointed high uncertainty were excluded; this problem in the QuikSCAT database is discussed by several studies including Freilich and Vanhoff (2006) and Quilfen et al. (2007). Moreover, the few areas with very calm wind conditions inside the cyclone running window did not use satellite data.

3. Wave modelling

The surface winds selected for this paper together with the new databases constructed provide a total of six different wind inputs for the wave modeling: CFSR (original); CFSR calibrated using linear regression; SeaWinds (original); SeaWinds centered interpolated to 1-hour of time resolution; CFSR with satellite data blended within cyclones; and CFSR with ambient winds calibrated using linear regression and

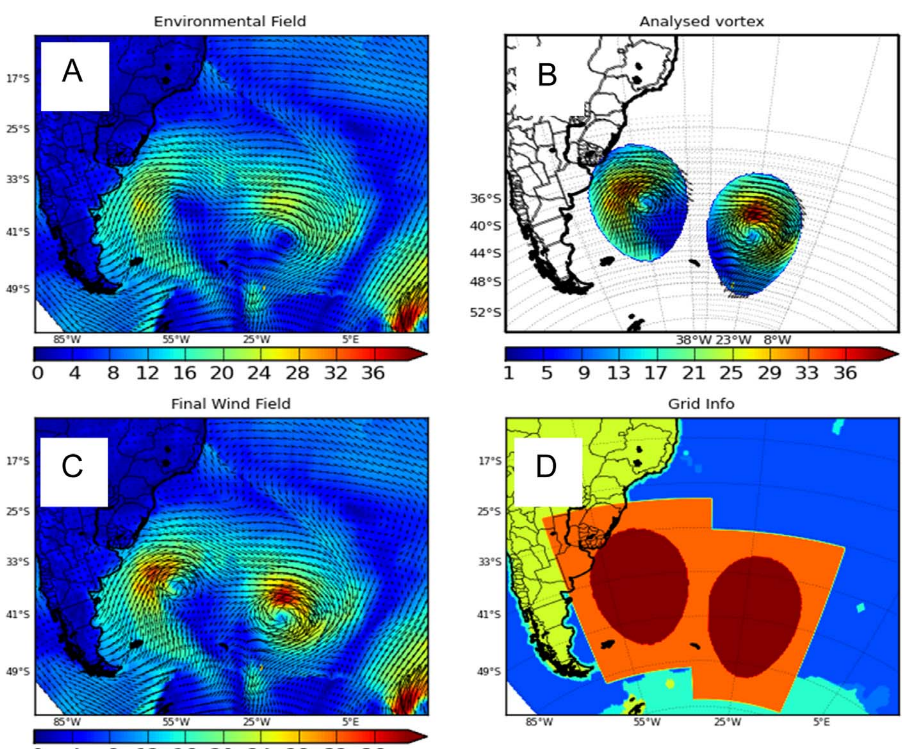

Fig. 7. Example of SeaWinds centered interpolation with two cyclones at 05Z on 27/07/2007. On the top left (A): ambient winds representing the background field (bi-linear interpolation). On the top right (B): Isolated cyclones (centered interpolation). Bottom left (C): Centered interpolated cyclones reinserted onto the background field. Bottom right (D): Grid information of the final wind fields where in blue is the area where SeaWinds were bi-linearly interpolated, and in dark orange is where the centered interpolation was applied. (For interpretation of the references to colour in this figure legend, the reader is referred to the web version of this article.)

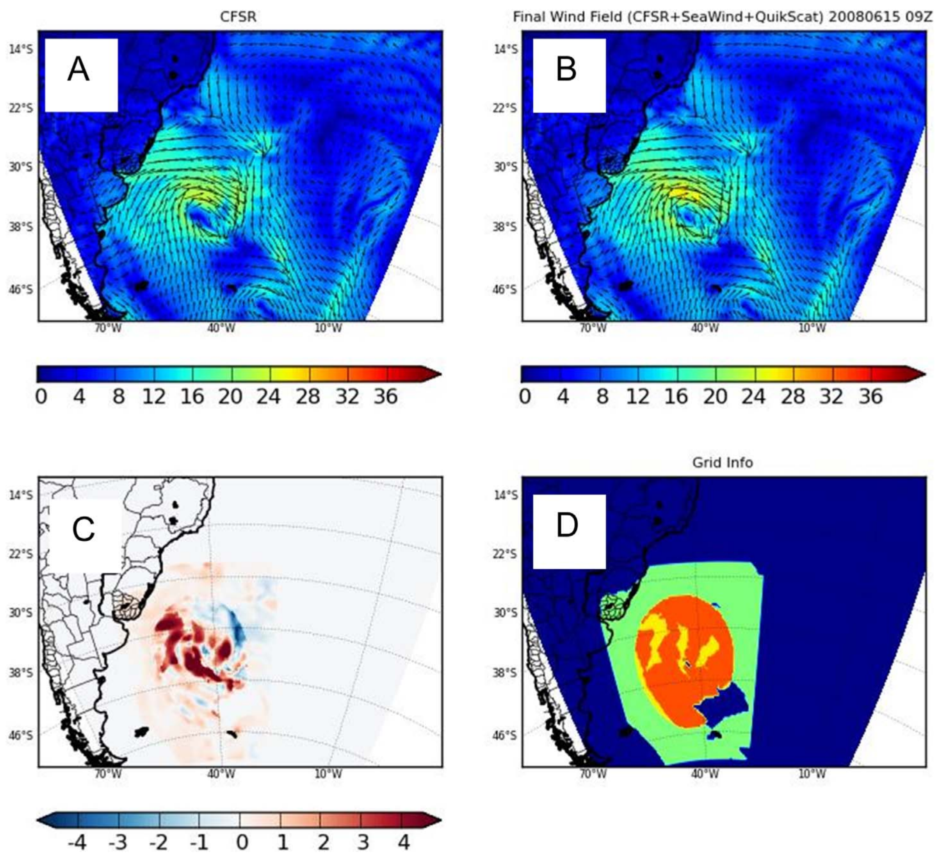

Fig. 8. Example of CFSR cyclonic winds merged with SeaWinds and QuikSCAT data, on 15/06/2008. On the top left (A): original CFSR wind. On the top right (B): Blended wind field with CFSR for non-cyclonic areas and SeaWinds/QuikSCAT inside the cyclone. Bottom left (C): difference between the new blended wind field minus CFSR wind. Bottom right (D): Grid information where in blue is the original CFSR, in dark orange the QuikSCAT wind, in yellow the SeaWinds and in green the transitioning area. (For interpretation of the references to colour in this figure legend, the reader is referred to the web version of this article.)

satellite data blended within cyclones. These winds lead to six wave hindcasts followed by an additional test retuning the input source term S_{in} in the wave model. Results are then evaluated and calibration and tuning are discussed. Altimeter data allows a spatial evaluation of the results, but comes with the problem of the coarse time sampling at single points. Satellites only revisit a site once every 10–35 days, and their tracks are separated by 100–200 km (Cooper and Forristall, 1997). The buoy has regular hourly measurements that better capture the time evolution and the peaks of the storms but does not provide any information about the spatial distribution. The use of both, satellites and buoys, provides sufficient information to evaluate the wave hindcasts in function of space and sea severity.

3.1. Wave hindcasts construction

The state-of-the art WAVEWATCH III model version 4.18 (Tolman et al. 2014), with the ST4 source-term package developed by Ardhuin et al. (2010) was selected for the wave simulations in the present paper. WAVEWATCH III is a third generation wave model that has been developed at NOAA/NCEP and provides an appropriate framework for the current investigation. The choice of the (ST4) package overs (ST2, Tolman and Chalikov, 1996) was justified on the basis of studies by Ardhuin et al. (2010) and Alves et al. (2014). It has the wind input source term S_{in} adapted from Janssen (1991) with adjustments performed by Bidlot et al. (2005, 2007). The complete wind input source term from Ardhuin et al. (2010) is given:

$$S_{in}(k,\theta) = \frac{\rho_a}{\rho_w}\frac{\beta_{max}}{\kappa^2}e^Z Z^4\left(\frac{u_*}{C}\right)^2 \times max\,[\cos(\theta-\theta_u),0]^2\ \ \sigma\ F(k,\theta) \tag{7}$$

where ρ_a and ρ_w are the air and water densities, β_{max} is a nondimensional growth parameter, κ is von Karman's constant, u_* is the wind friction velocity, C is the phase velocity and Z the effective wave age. Tolman et al. (2014) provide optimized parameters values for four tests. Using CFSR/NOAA input winds the best results are found with $\beta_{max} = 1.33$ according to Tolman et al. (2014). From Eq. 7 it is possible to see that S_{in} is directly proportional to β_{max} and to the energy of the spectrum. Therefore, higher values of β_{max} lead to higher significant wave heights – which can be applied as an attempt to reduce the underestimation of WAVEWATCH III simulations under extreme events, as seen in Fig. 1. Four different values of β_{max} were used in the wave modeling in this paper; the default value 1.33 (suggested by Tolman et al., 2014), plus three higher values of 1.44, 1.55 and 1.66 – applied to the original CFSR wind database to force the wave model. The impact of these four different β_{max} on the skill of the model is analyzed and further discussed below.

The WAVEWATCH III simulations were run using two grids, generated by a grid generation package (GridGen; Chawla and Tolman, 2007), where the bathymetry is based on Etopo1 (Amante and Eakins, 2009 - National Geophysical Data Center/Geodas Databases NGDA/GEODAS/NOAA) shown at Fig. 9, and the obstruction grids are generated using the GSHHS shoreline database (Wessel and Smith, 1996). The global grid has a resolution of 0.5° X 0.5° and it was forced with CFSR winds solely to obtain the boundary conditions to the sub-grid. The second grid has limits shown by Fig. 9, with resolution of 12′ X 12′ and it was forced by the six wind databases constructed and described. Both grids had the same input sea-ice concentration database of CFSR (Wu and Grumbine, 2013; Saha et al., 2000). The spectral information in WAVEWATCH III was set with: frequency increment factor, first frequency (Hz), number of frequencies, and number of directions, respectively:

1.124398 0.04177 25 36

Therefore, each spectrum is composed of a matrix with 25 frequencies and 36 directions. As the model is intended to simulate waves with a period of no more than 24 seconds, the first frequency is 0.04177 Hz.

The hindcast duration matches the full years of the wind databases,

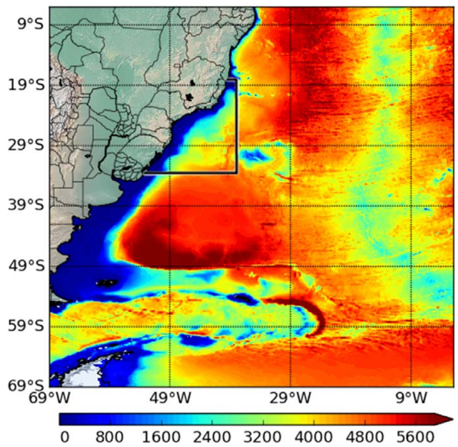

Fig. 9. Domain and bathymetry, in meters, of the sub-grid. The straight line borders in black indicate the region where buoy data was available (see Fig. 2). (For interpretation of the references to colour in this figure legend, the reader is referred to the web version of this article.)

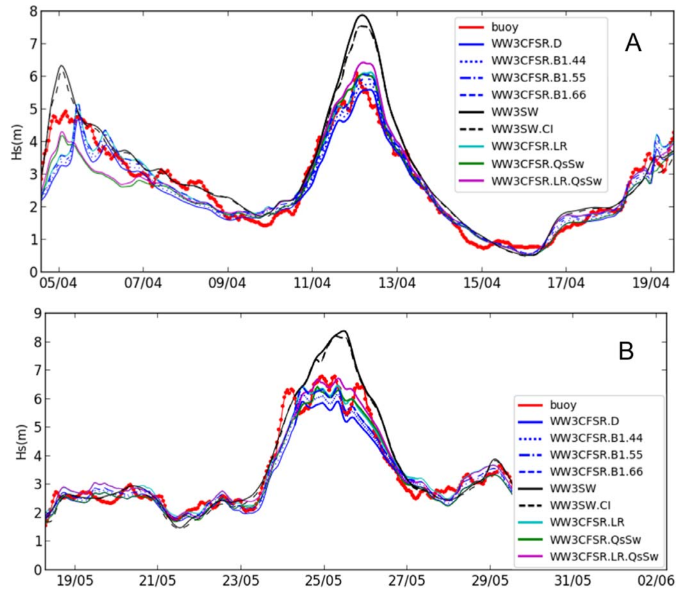

Fig. 10. Example of significant wave height (meters) from the nine wave hindcasts compared to a buoy at 32.86°S / 50.89°W moored in deep water, plotted in red. Solid Blue: WW3CFSR.D; Dotted Blue: WW3CFSR.B1.44; Dashed-Dotted Blue: WW3CFSR.B1.55; Dashed Blue: WW3CFSR.B1.66; Cyan: WW3CFSR.LR; Green: WW3CFSR.QsSw; Magenta: WW3CFSR.LR.QsSw; Solid Black: WW3SW; Dashed Black: WW3SW.CI. Top figure (A) shows an extreme event on 12/04/2003 when Hs reached 6.26 m with Tp 8.8 s. Bottom figure (B) occurred on 25/05/2003 when Hs reached 6.93 m and Tp 16.0 s. (For interpretation of the references to colour in this figure legend, the reader is referred to the web version of this article.)

which correspond to the period from 2002 to 2008; i.e., 7 years of simulation. The significant wave height (Hs) is the parameter analyzed, and the results assessment is performed using altimeter data, within the southwest Atlantic sub-grid of Fig. 9, and buoy data. A buoy at 32.86°S / 50.89°W (buoy 1 of Fig. 2), moored in deep waters in the south of Brazil, contains the longest and most reliable data and therefore is used as the main data source for the wave hindcasts evaluation. The same analysis was initially applied to a few other buoys in the region (additional buoys at Fig. 2) but the small number of measurements and the frequent errors captured by the quality control algorithm at these additional locations led to the exclusion of these data. Due to its southernmost location, buoy 1 was more exposed to the extreme events, which made it the most suitable for our analyses.

The description of the nine hindcasts is presented by Table 3. The hindcast WW3CFSR.D, run with original CFSR winds and default WAVEWATCH III parameters (no wind or wave calibration method applied), is used as the control dataset taken as reference in the analyses and comparisons. Hindcasts WW3CFSR.B1.44, WW3CFSR.B1.55 and WW3CFSR.B1.66 are the same as WW3CFSR.D but run with increasing β_{max} parameters of Eq. (7), which is a simple wave model tuning test. The hindcasts assessment is conducted under general and extreme conditions. The evaluation using buoy data also studies the error as a function of the sea-state severity (increasing percentiles) and looks at individual extreme events.

A first example of modeled Hs compared to buoy measurements for two extreme events in the south of Brazil is shown in Fig. 10. The hindcasts are plotted from now on using the same style: WW3CFSR.D (solid blue), WW3CFSR.B1.44 (dotted Blue), WW3CFSR.B1.55 (dashed-dotted blue), WW3CFSR.B1.66 (dashed blue), WW3CFSR.LR (cyan), WW3CFSR.QsSw (green), WW3CFSR.LR.QsSw (magenta), WW3SW (solid black), WW3SW.CI (dashed black). Both events were generated by intense cyclones in the South Atlantic Ocean and the observations exceeded 6.0 m of significant wave height at the peak of the storms. Although Fig. 10 presents only two events - a low statistical relevance from which one cannot draw any conclusion – it is a good introductory example of the hindcasts features under severe conditions. From Fig. 10A and B it is clear that hindcasts are very similar each other for small waves, being in good agreement with measurements. The dispersion among the nine hindcasts increases significantly for higher waves, especially during the peak of the storms, when the difference to the buoy measurements becomes large. At this moment, the black lines (hindcasts forced with SeaWinds database) tend to overestimate the peaks, while the blue solid line (WW3CFSR.D) underestimates it. This is a common characteristic visualized in most of the extreme events analyzed and it is confirmed throughout this study. Another characteristic can be exemplified in the beginning of Fig. 10A, on 05/04/2003, regarding a less severe event. The wave hindcasts forced with satellite winds (WW3CFSR.QsSw, WW3CFSR.LR.QsSw, WW3SW, WW3SW.CI) tend to better follow the wave measurements, even when under- or over-estimated, which leads to a better correlation coefficient compared to purely CFSR forcing winds hindcast.

The input winds associated with the extreme wave event of Fig. 10B is presented by Fig. 11. Although the wind direction and circulation is very similar among wind databases, the satellite winds show higher intensities when compared to CFSR. Hence, the CFSR.QsSw wind

Table 3
Description of the nine wave hindcasts constructed.

1 WW3CFSR.D	Default hindcast <u>used as reference</u>. WW3 run with original CFSR wind reanalysis and β_{max} = 1.33.
2 WW3SW.CI	WW3 run with SeaWinds with cyclones centered interpolated. Final time resolution of 1 h
3 WW3CFSR.LR	WW3 run with CFSR winds calibrated using a linear regression function, applied to the entire grid and data.
4 WW3CFSR.QsSw	WW3 run with CFSR winds merged with satellite data (QuikSCAT and SeaWinds) inside the cyclones only.
5 WW3CFSR.LR.QsSw	WW3 run with the combination of CFSR.LR and CFSR.QsSw winds. The linear regression function is applied to the entire grid apart from the cyclonic areas, where satellite data is blended.
6 WW3SW	WW3 run with original SeaWinds satellite database.
7 WW3CFSR.B1.44	WW3 run with original CFSR wind reanalysis and β_{max} = 1.44.
8 WW3CFSR.B1.55	WW3 run with original CFSR wind reanalysis and β_{max} = 1.55.
9 WW3CFSR.B1.66	WW3 run with original CFSR wind reanalysis and β_{max} = 1.66.

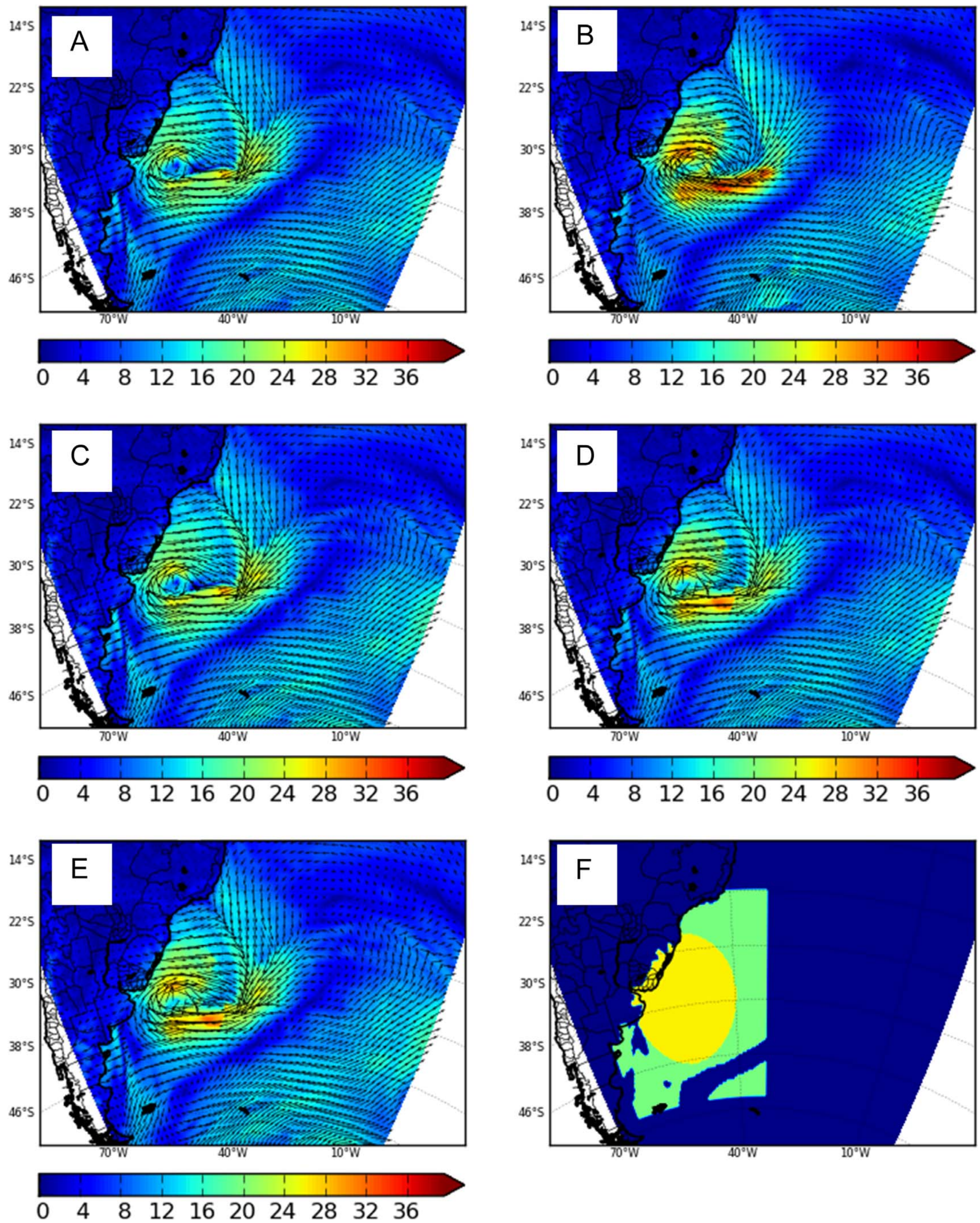

Fig. 11. Surface wind fields (m/s) on 24/05/2003, which generated the event of Fig. 10B. A: Original CFSR reanalysis. B: SeaWinds centered interpolated (SW.CI). C: CFSR calibrated using a linear regression function (CFSR.LR). D: CFSR with satellite data blended inside the cyclones (CFSR.QsSw). E: Composition of D and E, with linear regression applied to the entire CFSR reanalysis apart from the cyclonic areas where satellite data is used (CFSR.LR.QsSw). F: Grid information where in blue is the original CFSR, in yellow the satellite data and in green the transitioning area. (For interpretation of the references to colour in this figure legend, the reader is referred to the web version of this article.)

database have much stronger winds inside the cyclone than CFSR winds, and have exactly the same winds of CFSR for non-cyclonic regions identified by Fig. 11F. Fig. 12 presents the significant wave height generated by the winds of Fig. 11. It confirms the direct impact of wind under- and over-estimation on the wave fields. Fig. 12A has the smallest waves due to the lowest intensities of original CFSR winds of Fig. 11A. On the other hand, satellite winds inside the cyclones (Fig. 11B,D,E) result in larger waves in the cyclone fetch. The simple linear regression wind calibration of Fig. 11C increases the intensities of the whole domain by a small amount, which leads to Hs within the cyclone that is greater than WW3CFSR.D but smaller than the wave hindcasts forced with satellite winds. It can be confirmed by comparing Fig. 12C and Fig. 12D. The linear regression (Fig. 12C) also amplifies the waves in non-cyclonic areas seen in the eastern part of the map, which is higher than Fig. 12D for the same location. However, the cyclonic waves of Fig. 12D are higher than in Fig. 12C.

In order to better visualize the differences between hindcasts, Fig. 13 shows the difference of each hindcast compared to the reference WW3CFSR.D, for the same instant of Fig. 11 and Fig. 12. Hot colors in red indicate locations where constructed hindcasts have higher waves

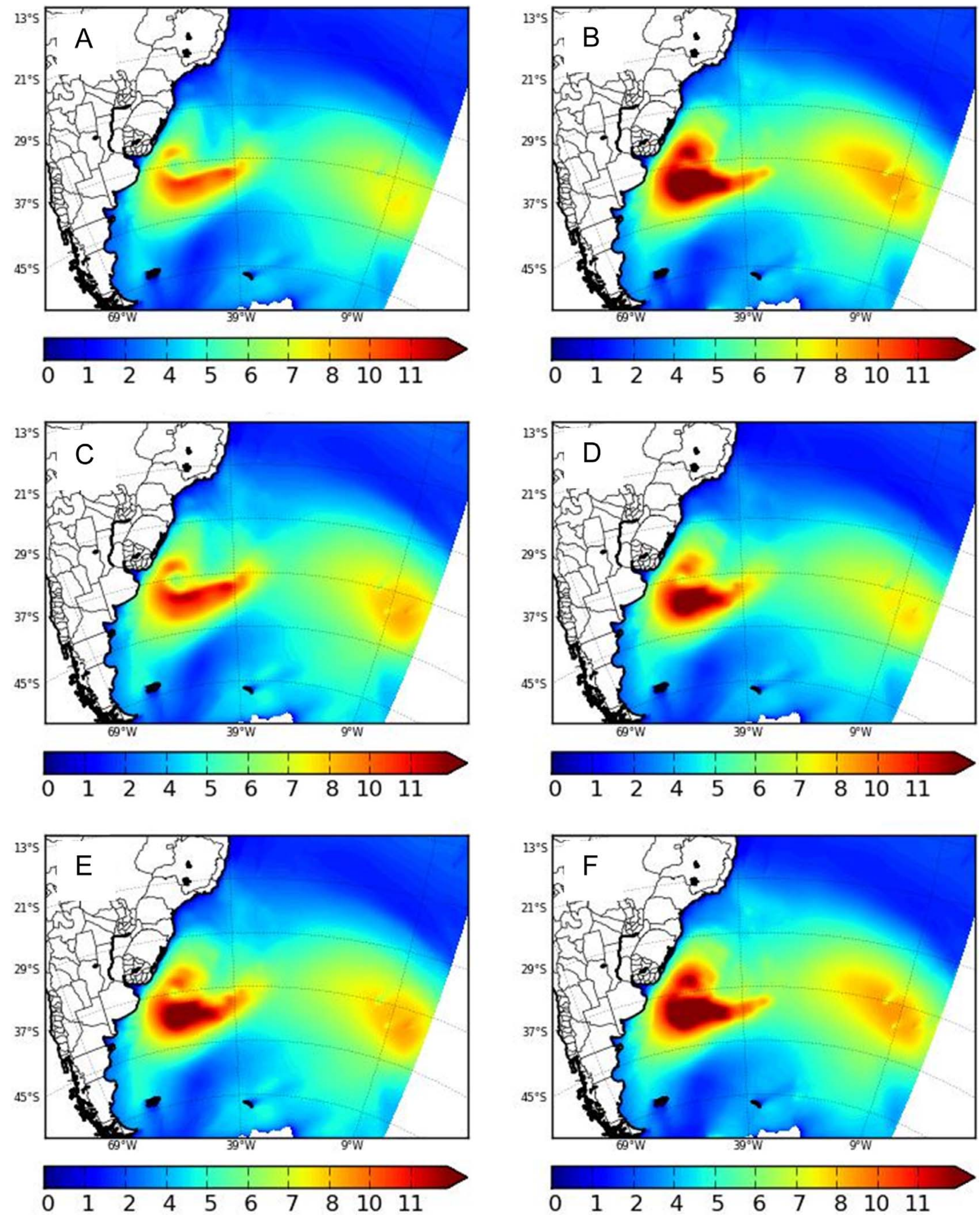

Fig. 12. Significant wave height (meters) for the wind inputs of Fig. 11, on 24/05/2003, the same event of Fig. 10B. A: WW3CFSR.D; B: WW3SW.CI; C: WW3CFSR.LR; D: WW3CFSR.QsSw; E: WW3CFSR.LR.QsSw; F: WW3SW.

than the default WW3CFSR.D, whereas cold colors in blue indicate locations where the constructed hindcasts have smaller waves. This plot highlights the impact of using satellite wind data compared to the linear regression uplift. Fig. 13B confirms the large overestimation of waves generated by SeaWinds. Fig. 13C shows the overall increase of wave heights in the whole domain using the linear regression wind calibration, which is much smaller than the increase of the wave heights inside the cyclones forced by satellite winds. Fig. 13D illustrates that the impact of WW3CFSR.QsSw is mainly restricted to cyclonic areas. The differences in the wave fields of Fig. 13 spreads out of the wave generation zone, moving dispersively towards the south coast of Brazilian where the buoy was moored (Fig. 2A), which explains the hindcast divergences of Fig. 10B.

3.2. Bulk evaluation for general conditions

The altimeter database used for the hindcast assessment was quality controlled and organized by the GlobWave Project (Ash et al., 2012), an initiative funded by the European Space Agency (GlobWave/DD/PUG. GLOBWAVE Product User Guide, 2013). Due to the period of simulations from 01/2002 to 12/2008, the exact missions used for the evaluation were: JASON1, JASON2, TOPEX/Poseidon, GEOSAT, ERS2 and ENVISAT. The composition of data pairs WAVEWATCH / satellite first excludes areas close to the coast and in shallow waters, as recommended by GlobWave/DD/PUG (2013). The satellite data track is assigned to the nearest WAVEWATCH regular grid point, taking the sub-grid of 12′ X 12′, and the WAVEWATCH significant wave heights

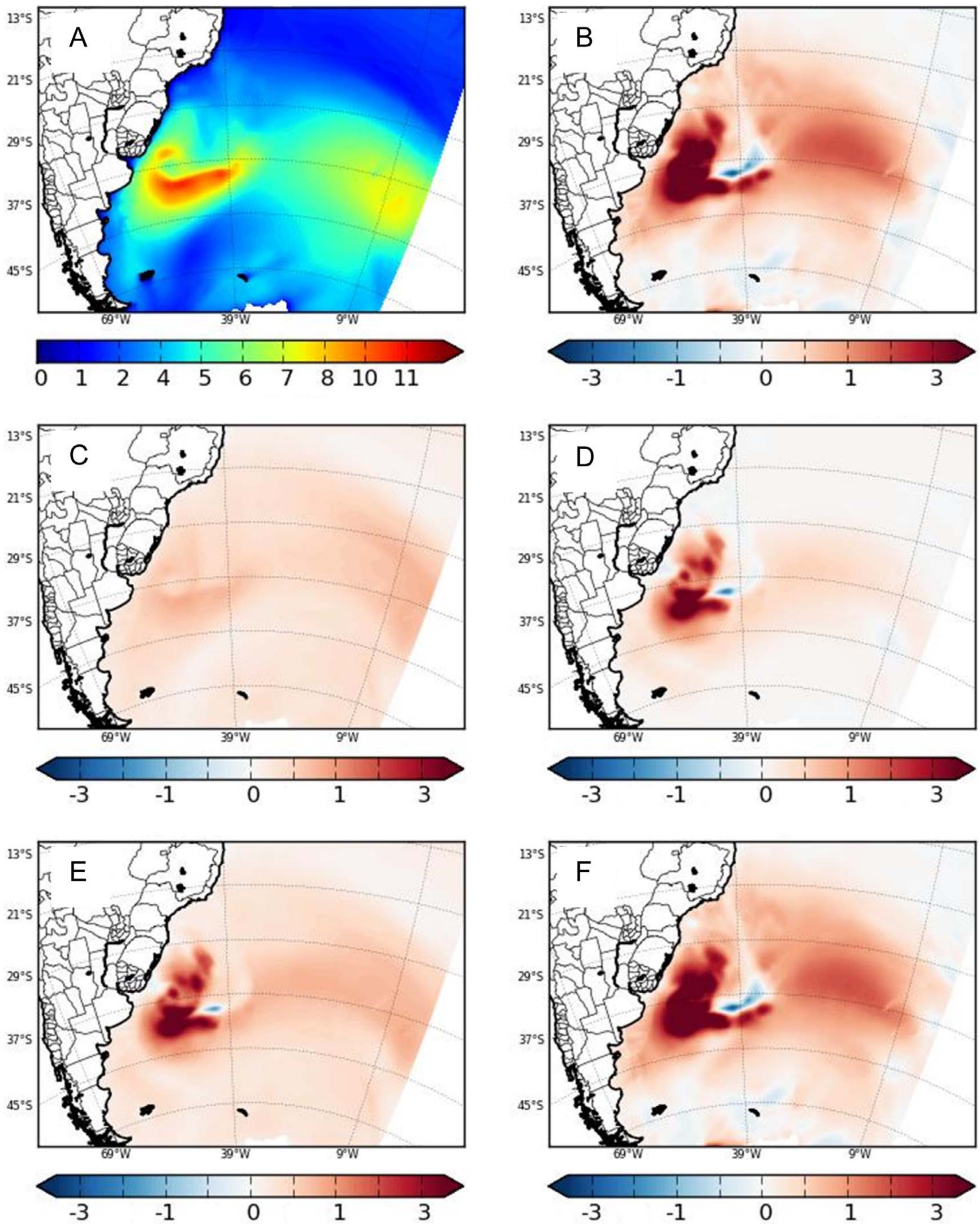

Fig. 13. Differences (meters) between the significant wave heights forced with wind fields other than CFSR (Fig. 12B,C,D,E,F) minus the simulation using the original CFSR as the reference (WW3CFSR.D, plotted in Fig. 12A) on 24/05/2003. A: Wave field of WW3CFSR.D, same as Fig. 12A. B: WW3SW.CI - WW3CFSR.D; C: WW3CFSR.LR - WW3CFSR.D; D: WW3CFSR.QsSw - WW3CFSR.D; E: WW3CFSR.LR.QsSw - WW3CFSR.D; F: WW3SW - WW3CFSR.D. Hot colors plotted in red indicate regions where the new hindcast has higher wave heights than WW3CFSR.D, whereas cold colors in blue show regions where WW3CFSR.D is higher. (For interpretation of the references to colour in this figure legend, the reader is referred to the web version of this article.)

are interpolated in time to match the satellite data. Since the WAVEWATCH regular grid has a high resolution of 12′ X 12′ and 1 h, it ensures that wave model results and satellite measurements have distance of maximum 8.5′ and 0.5 h A large group of pairs were constructed and, for the visualization, it was assembled to a new grid with resolution of 1° X 1° This procedure partially followed the description of Young and Holland (1996) who, differently, partitioned the satellite data into 2° X 2° sampling squares. Results are illustrated by Fig. 14, where hot colors in red at the bias maps indicate regions where the significant wave heights from the satellite are greater than the hindcasts, i.e., the wave heights from hindcast are underestimated. Cold colors in blue indicate regions where the hindcast overestimates the satellites.

The first feature clearly noticeable is the great difference in accuracy among locations, with a strong variation with longitude. All hindcasts have relative higher waves at eastern portions of the South Atlantic Ocean than at western locations, close to South America. This leads to overestimation of all hindcasts in the south-east areas and underestimation of some hindcasts at western locations. The default hindcast WW3CFSR.D (Fig. 14A) presented the largest underestimation in Brazil at southern states, but still containing small bias, around 0.2 m in average. The increase of wind intensities using the linear regression calibration of WW3CFSR.LR resulted in an uplift of the wave heights

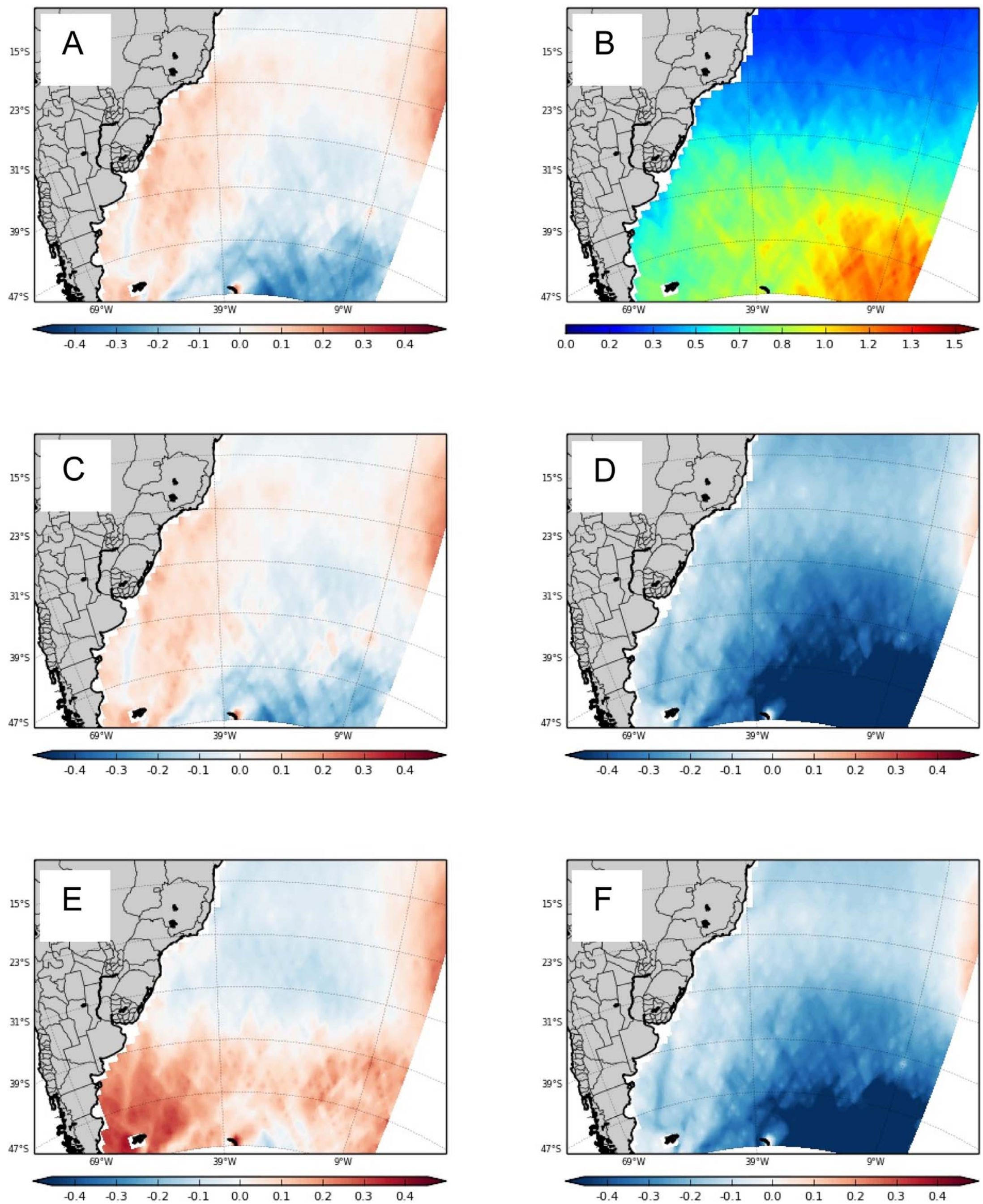

Fig. 14. Comparison between the original CFSR wind intensity with calibrated fields. A) CFSR Mean error ME; B) CFSR root mean squared error (RMSE). C) Mean error of WW3CFSR.QsSw; D) Mean error of WW3CFSR.LR. E) Mean error of WW3SW.CI and F) Mean error of WW3CFSR.B1.66.

throughout the entire grid (Fig. 14D). This benefits the western areas removing their underestimation but it worsens the overestimation at south-east grid points. We will later show that the deterioration of the simulation at western portions of the ocean, although distant from Brazil, compromise other error metrics, as the correlation coefficient, when evaluated against buoy measurements. The inclusion of satellite data within the cyclones, in WW3CFSR.QsSw (Fig. 14C), presents a small impact, in average, when compared to the default hindcast WW3CFSR.D. It is possible to see a small improvement and reduction of both positive and negative bias, especially at mid-latitudes and southern grid points where the influence of cyclones is greater. The hindcast fully forced by satellite winds, WW3SW.CI (Fig. 14E), has a different pattern, where the bias significantly changes with the latitude. The underestimation of WW3SW.CI is more evident at the southern points whereas the mid and northern locations of the figure, including Brazil, present small overestimation. The increase of β_{max} from 1.33 (used by WW3CFSR.D) to 1.66, showed an improvement in terms of accuracy at Brazilian waters but it severely increases the problem of overestimation at western areas. This effect is similar to the linear regression uplift of the winds in WW3CFSR.LR. Moreover, hindcasts WW3CFSR.B1.66 and WW3CFSR.LR also deteriorates the root mean square errors compared to WW3CFSR.D. Therefore, even if they present better results for extreme waves, the worse accuracy in averaged and moderate highs disregards the main purpose of this paper; which is to improve the simulation of extreme waves without compromising the general conditions.

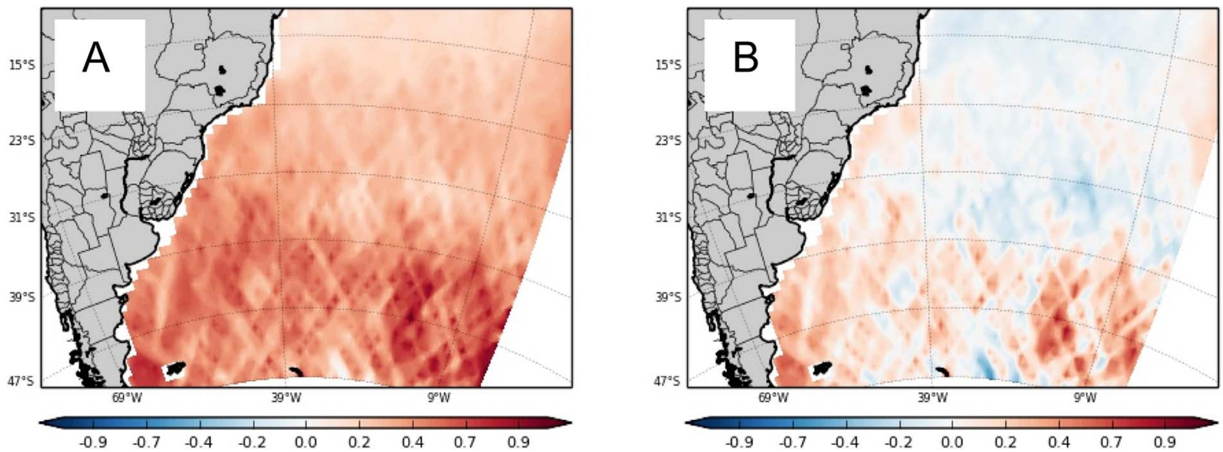

Fig. 15. Mean error (ME), in meters, of the hindcasts against altimeter data for the events above the 80th percentile of significant wave height. Left: WW3CFSR.D. Right: WW3CFSR.LR.QsSw.

3.3. Evaluation under severe conditions

This section will progressively move the analysis to more severe events, selecting higher percentiles. First, using altimeter data, the analysis is redone for waves above the 80th percentile. Then, an evaluation using buoy measurements calculates the bias in function of the percentile, from 0 to 99th. The last part concludes the hindcast evaluation by analyzing the errors associated with the 20 most extreme events registered by the buoys. We will see that, depending on the level selected and the error metric considered, the group of best hindcasts can change.

Fig. 15 presents the most important results, which is worthwhile to compare it with Fig. 14A. The colorbar scale has now changed and broadened the values, which clearly shows the increase of hindcast errors under severe conditions. The deterioration of hindcast is mainly found at mid and southern latitudes. Although the largest errors are more evident at these locations, the propagation of the hindcast errors towards northern latitudes worsens the results across the entire domain. The deterioration of hindcasts under severe conditions moves toward the underestimation of the simulations compared to the measurements, as illustrated for the dataset WW3CFSR.D in Fig. 15A. The use of satellite winds inside the cyclones (WW3CFSR.QsSw) presented a small improvement compared to WW3CFSR.D, considering these range of percentiles analyzed and averaged. The wave hindcast WW3CFSR.LR that severely overestimated altimeter waves in the comparison for general conditions has now presented small bias, with similar effect of increasing the parameter β_{max}. Fig. 15B shows the best results related to the hindcast WW3CFSR.LR.QsSw, with the combined application of the linear regression wind calibration together with satellite wind data inside the cyclones. The linear regression reduced the general bias while the satellite data within cyclones improve the results at mid and southern latitudes. The bias at Fig. 15B is in between 0.2 and 0.4 m, and locations close to Brazil show very small errors.

The averaged analysis above the 80th percentile used so far cannot be considered ¨extreme¨. However, the use of higher percentiles would compromise the statistics and lead to small satellite samples. Regarding the wave buoy, containing a better sampling rate, it is possible to move to higher percentiles. The mean error was calculated several times, resampling the buoy and hindcast data by fixing thresholds linked to the percentiles, from 0 to 99. The error metrics is then calculated and averaged for all dataset with wave heights above each of these percentiles. In other words, Fig. 16 is built by re-sampling the data moving a minimum percentile level from 0 to 99 and calculating the metrics, with several iterations that generate error metrics values and the curves. It is now possible to evaluate the hindcast errors for each level of severity, from small waves until extreme events above the 95th

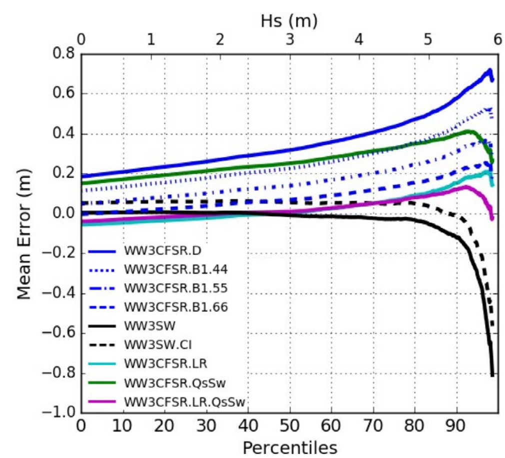

Fig. 16. Direct evaluation of the nine wave hindcasts against buoy measurements at 32.86°S / 50.89°W, in function of the sea severity. Mean error (meters) of significant wave height versus percentiles (and corresponding value of significant wave height on top axis). Solid Blue: WW3CFSR.D; Dotted Blue: WW3CFSR.B1.44; Dashed-Dotted Blue: WW3CFSR.B1.55; Dashed Blue: WW3CFSR.B1.66; Cyan: WW3CFSR.LR; Green: WW3CFSR.QsSw; Magenta: WW3CFSR.LR.QsSw; Solid Black: WW3SW; Dashed Black: WW3SW.CI. (For interpretation of the references to colour in this figure legend, the reader is referred to the web version of this article.)

percentile. Once again, positive values indicate underestimation of hindcasts related to the buoy, while negative values indicate overestimation of hindcasts. The default hindcast WW3CFSR.D is shown in solid blue in Fig. 16, presenting the largest underestimation (positive mean error) compared to the buoy for all percentiles. The increase of WAVEWATCH parameter β_{max} reduces the underestimation, as observed in the dotted, dashed-dotted and dashed blue lines. However, this led to the overestimation of WW3CFSR.B1.66 at the lower percentiles, and did not avoid the increase of error at higher percentiles, which is the most critical problem of simulations. It is also observed in the hindcast WW3CFSR.LR, with similar shape of the error evolution. The percentiles from 0 to 40% are overestimated while the underestimation increases moving towards the extreme events. The opposite occurs with hindcasts WW3SW and WW3SW.CI, forced by satellite winds. The errors increase dramatically at higher percentiles but related to overestimation, when the hindcasts present much higher waves than the buoy measurements. The dashed-black line, WW3SW.CI, shows a smaller overestimation than WW3SW; i.e., the centered interpolation of Tolman and Alves (2005) resulted in decrease of the wave heights.

The use of satellite winds inside the cyclones, WW3CFSR.QsSw, is shown by the green line of Fig. 16. It closely follows the blue line of

WW3CFSR.D for small and moderate waves, with a slight underestimation. However, above the 80th percentile, curves start to diverge and, especially above the 93rd percentile, the bias of WW3CFSR.QsSw drops while the WW3CFSR.D error keeps increasing. The shape of this drastic reduction of the WW3CFSR.QsSw error curve is similar to the WW3SW and WW3SW.CI hindcasts, entirely forced by satellite winds. The hindcast WW3CFSR.LR.QsSw (in magenta at Fig. 16) shows small bias for all ranges of percentiles, with the combination of the linear regression for non-cyclonic areas and scatterometer winds within cyclones. WW3CFSR.LR.QsSw has a small overestimation at small percentiles, similar to WW3CFSR.LR, and it presents the same reduction of bias for extreme events seen in the WW3CFSR.QsSw curve.

The last part of the wave hindcasts assessment is focused on the twenty most extreme events registered by the same heave-pitch-roll buoy 1 from 05/2002 to 10/2004. The independent events were selected considering 36 hours before and after the instant of maximum wave height from the buoy – selecting slices of 72 hours of hindcast and buoy data. Although events have different durations, the same period is used for all extremes in order to calculate the correlation coefficient with the same data length. The differences from the buoy to the hindcast, at the peak of the storm (even when displaced), is also computed, referred as *PeakErr*. Table 4 presents the results, where ME, RMSE and PeakErr are given in meters. Besides, Fig. 17 presents a Taylor Diagram (Taylor, 2001) containing each of the twenty events simulated by the hindcasts and compared against the buoy. Table 4 shows positive mean errors (underestimation) for all hindcasts apart from WW3SW and WW3SW.CI, which overestimated the buoy measurements. Although the small bias of WW3SW.CI, it shows the worst RMSE, 0.5 m, and the worst correlation coefficient of 0.92. The largest underestimation is found in WW3CFSR.D, considering both ME and *PeakErr*. It gradually decreases to better results with increasing β_{max} parameters. The hindcast WW3CFSR.LR has good results for the ME, RMSE, SI and *PeakErr*, but the correlation coefficient (CC) is practically the same as WW3CFSR.D. The results of WW3CFSR.QsSw show a small improvement in the ME, RMSE, SI and PeakErr metrics compared to WW3CFSR.D, and it has the best CC among all hindcasts, of 0.95. The hindcast WW3CFSR.LR.QsSw presents good overall results, with very small bias, small RMSE and SI and the second best CC.

In order to evaluate the new constructed hindcasts, Table 5 was made with the percentage of improvement, for each error metric, related to the control hindcast WW3CFSR.D. Positive values indicate better result of the constructed hindcast than WW3CFSR.D, whereas negative values point to deterioration of the new hindcast compared to WW3CFSR.D. The group of hindcasts that better reduced the bias (ME and PeakErr) for extreme events is composed of: WW3SW.CI, WW3CFSR.LR.QsSw, WW3CFSR.LR and WW3CFSR.B1.66. The group that better reduced the RMSE and SI is: WW3CFSR.LR, WW3CFSR.LR.QsSw and WW3CFSR.B1.66. The hindcast WW3SW.CI though presented deterioration of RMSE. The hindcasts with the best improvement in CC are: WW3CFSR.QsSw and WW3CFSR.LR.QsSw. The hindcasts WW3SW.CI and WW3CFSR.B1.66 showed worse correlation coefficients than the default WW3CFSR.D.

Table 4
Average of error metrics of the nine wave hindcasts for the twenty most extreme events measured by the buoy, at 32.86°S / 50.89°W. PeakErr is the difference of significant wave height from the buoy minus the significant wave height from the hindcasts, for the peak value of the event (maximum significant wave height).

	ME	RMSE	SI	PeakErr	CC
WW3CFSR.D	0.394	0.498	0.136	0.685	0.930
WW3SW.CI	−0.031	0.503	0.134	−0.031	0.922
WW3CFSR.LR	0.052	0.292	0.078	0.186	0.931
WW3CFSR.QsSw	0.245	0.409	0.112	0.505	0.948
WW3CFSR.LR.QsSw	0.036	0.325	0.086	0.225	0.944
WW3SW	−0.146	0.498	0.131	−0.242	0.932
WW3CFSR.B1.44	0.282	0.403	0.111	0.505	0.932
WW3CFSR.B1.55	0.177	0.335	0.092	0.336	0.930
WW3CFSR.B1.66	0.094	0.297	0.081	0.196	0.929

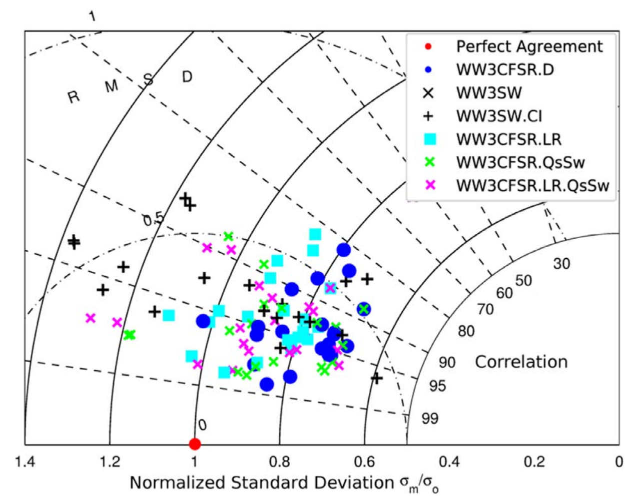

Fig. 17. Taylor Diagram (BLT) for the twenty most extreme events measured by a buoy at 32.86°S / 50.89°W. Blue circle: WW3CFSR.D; Cyan square: WW3CFSR.LR; Green x: WW3CFSR.QsSw; Magenta x: WW3CFSR.LR.QsSw; Black x: WW3SW; Black+: WW3SW.CI. The red circle represents the perfect agreement, with RMSE equal to zero, correlation coefficient equal to one, and normalized standard deviation equal to one. (For interpretation of the references to colour in this figure legend, the reader is referred to the web version of this article.)

Table 5
Percentage of improvement of the new hindcasts compared to the reference WW3CFSR.D for the twenty most extreme events measured by the buoy, at 32.86°S / 50.89°W.

	ME(%)	RMSE(%)	SI(%)	PeakErr (%)	CC(%)
WW3SW.CI	92.13	−1.00	1.47	95.47	−0.86
WW3CFSR.LR	86.80	41.36	42.65	72.85	0.11
WW3CFSR.QsSw	37.81	17.87	17.67	26.28	1.93
WW3CFSR.LR.QsSw	90.86	34.74	36.76	67.15	1.50
WW3SW	62.94	0.00	3.68	64.67	0.21
WW3CFSR.B1.44	28.43	1.00	18.38	26.28	0.21
WW3CFSR.B1.55	55.08	32.73	32.35	50.95	0.00
WW3CFSR.B1.66	76.14	40.36	40.44	71.39	−0.11

Instead of showing averages among the twenty events, Fig. 17 has the results for each extreme event plotted with the Taylor Diagram (BLT). Points on the right of the curve of normalized standard deviation equal to 1.0 have underestimated the buoy measurements, while points on the left of this curve indicate overestimation of the wave heights. The RMSE are represented by the two dashed-dotted black curves, in meters, and the correlation coefficient by the straight rays in dashed black. It is first clear to note a great spread of the results, all hindcasts have events very well simulated and others with larger errors. The cloud of blue dots indicates WW3CFSR.D with majority of underestimation and only one event overestimated; whereas the black markers (WW3SW and WW3SW.CI) mostly overestimate the measurements. The green marker, WW3CFSR.QsSw, shows a better correlation coefficient but a large spread over the normalized standard deviation. It is important to note that the green and magenta markers, related to WW3CFSR.QsSw and WW3CFSR.LR.QsSw, are the only ones bellow the curve of RMSE of 0.5 m, which highlights the benefit of using satellite winds within cyclonic areas. Fig. 10A and B presented two of these twenty extreme events which were very well simulated by the hindcast WW3CFSR.LR.QsSw – considered one of the best among the nine hindcasts constructed. It also illustrates the common overestimation and small correlation with the measurements of the hindcasts entirely forced by satellite winds. In addition to Fig. 10, there are other events at Fig. 17 that could exemplify and show some benefits of the calibrations performed in this study.

4. Conclusions

This paper investigates three types of surface-wind product calibration and their impact to nine wave hindcasts constructed using a state-of-the art numerical wave model. Two calibration approaches are related to the surface-wind product enhancements: a simple linear regression applied to the CFSR wind intensities, and a method of blending scatterometer wind within cyclonic areas. The third calibration method is a retuning of S_{in} in the wave model, with the increase of the wind-input source term parameter β_{max}. These three groups of wave hindcasts were evaluated using altimeter and buoy data for general and severe conditions, considering the main goal of improving the wave modeling in the South Atlantic Ocean and Brazil under extreme events, without compromising the average conditions.

The evaluation maps using altimeter data highlight the great spatial differences in the alternative hindcasts errors, with overestimation at eastern longitudes and underestimation close to South America. Hindcasts made by simply adjusting β_{max} to 1.66 or correcting the CFSR winds via linear regression deteriorate the root mean square errors and resulted in large bias, with overestimation at eastern portions of the ocean. However, at western areas of the South Atlantic Ocean, offshore Brazil, they reduced the underestimation of the waves, especially at higher percentiles. The error metrics and maps have shown that increasing the β_{max} parameter in WAVEWATCH III leads to similar results to increasing the input wind intensity with a linear regression. It is effective in reducing the average bias but has small or no impact on the root mean square error and the correlation coefficient. The comparison of bulk assessment under general conditions (Fig. 14) against severe conditions (Fig. 15A), together with the evaluation in function of the percentiles (Fig. 16), proves that the hindcast errors increase significantly with the sea-state severity. The linear regression of input winds and increase of β_{max} parameter are methods that do not correct the increase of bias with percentiles, which is the main goal of this study.

The evaluation of CFSR winds indicated errors between 0.5 to 1.0 m/s for calm to moderate conditions, while within extreme cyclones the underestimation of CFSR grows to values around 5 m/s. The linear regression applied generally increases in around 5% to 6% CFSR wind intensities. However, the process still retains an underestimation by CFSR of up to 25%, associated with the approximate 5 m/s differences within strong extra-tropical storms in the South Atlantic Ocean. Therefore, under cyclonic conditions, the proposed method of blending satellite-derived cyclonic wind fields with background CFSR data proves effective, leading to a better representation of winds both during ambient or extreme cyclonic conditions. Hence, the wave assessment using altimeter data showed the hindcast WW3CFSR.QsSw with small improvements related to the control hindcast WW3CFSR.D for general conditions. However, Fig. 16 clearly shows a progressive improvement of this approach with increasing percentiles, and a great reduction of the hindcast underestimation above the 93rd percentile, associated with waves greater than 5.5 m. The hindcast WW3CFSR.QsSw has also the benefit of not deteriorating the average conditions by worsening the overestimation at eastern latitudes. The improvement of the extreme cyclonic waves without compromising the general conditions leads to the better representation of the peak of the storms and higher correlation coefficient. It confirms the strong dependence of accurate simulation of extreme events to the surface wind inputs, as discussed by Cavaleri (2009).

The methodology of blending satellite winds in cyclonic areas, applied in hindcasts WW3CFSR.QsSw and WW3CFSR.LR.QsSw, is the only calibration approach among the three tested that was able to reduce the error as a function of increasing percentiles. However, even using much stronger cyclonic winds from satellite, the underestimation of the peaks is still noticeable in WW3CFSR.QsSw. This is associated with strong cyclones propagating eastwards that accumulate spectral energy on the local waves that propagate with the storm. This process, which is strongly-dependent on the background CFSR winds outside areas corrected by scatterometer data, cannot be well represented if the CFSR data is itself not corrected. Indeed, the extreme wave generation process occasionally extrapolates beyond the cyclonic area, following a larger fetch associated with southerly winds on the left of the trough, as shown above. Hence, the combination of the linear regression of non-cyclonic areas with the satellite data within the cyclones successfully generated a hindcast (WW3CFSR.LR.QsSw) with small errors offshore Brazil in all percentiles, from calm to extreme conditions. For the twenty most extreme events measured by a buoy in the South Atlantic near Brazil, the average bias of Hs at the peak of the storms was only 22 cm with scatter index of 0.086 and correlation coefficient of 0.94.

This study shows that the use of satellite and buoy data to build new wave hindcasts lead to a reduction of the wave underestimation of the peak of the extremes from 0.7 to 0.2 m, a decrease of percentage error from 14% to less than 8% and with new hindcasts containing the RMSE under extreme conditions below 0.5 m. We also highlight the importance of long and reliable measurements in the South Atlantic Ocean together with the implementation of a network of continuous oceanographic and meteorological data collection. The results of this study draws attention to the most important areas to be monitored for extreme waves (Fig. 5), which are the coasts of northeast Argentina, Uruguay and the southern states of Brazil. Finally, although the improvements in the extreme wave modeling performed in this paper, Fig. 17 and Table 4 shows that there is still space for more work, in order to continuously increase the accuracy of extreme events. Approaches that better capture the turbulent behavior of the air-sea interface during stormy events, followed by more complex non-linear approximation methods, could improve even more the simulation of extreme waves. The inclusion of peak period and other spectral information would also have a great benefit to the calibrations and analyzes. Additionally, data assimilation strategies applied to surface winds together with the inclusion of wave data assimilation could also further improve the results of this study. Finally, we suggest future studies to consider error metrics beyond the traditional bias, RMSE, scatter index and correlation coefficient, as discussed by Mentaschi et al. (2013) and Hanna and Heinold (1985).

Acknowledgments

This work was funded by Coordenação de Aperfeiçoamento de Pessoal de Nivel Superior (CAPES), a government agency linked to the Brazilian Ministry of Education, under the programme Ciência Sem Fronteiras. Authors would like to acknowledge CAPES as well as the agencies and institutions that provided the data for the present study, namely: National Centers for Environmental Prediction (NCEP/NOAA), National Aeronautics and Space Administration (NASA), National Environmental Satellite, Data, and Information Service (NESDIS/NOAA), National Climatic Data Center (NCDC/NOAA) and the Brazilian Navy with “Programa Nacional de Bóias” (PNBOIA, associated with GOOS-Brazil). The research developed was hosted by two institutions that we are grateful to acknowledge: Environmental Modeling Center (EMC/NCEP/NOAA) and Laboratório de Instrumentação Oceanográfica of Federal University of Rio de Janeiro (LIOC/PENO/COPPE UFRJ). Finally, we thank the technical support and data from the research center of PETROBRAS (TEO/CENPES/PETROBRAS) and Centro de Hidrografia da Marinha (CHM, Brazilian Navy). The third author holds a visiting position at COPPE/UFRJ, which is funded by Conselho Nacional de Pesquisa of Brazil (CNPq).

References

Alonso, R., Solari, S., Teixeira, L., 2015. Wave energy resource assessment in Uruguay. Energy 93 (683), 696.

Alves, J.H.G.M., Melo, E., 2001. Measurement and modeling of wind waves at the northern coast of Santa Catarina, Brazil. Revista Brasileira de Oceanografia 49 (1-2),

13–28 São Paulo.
Alves, J.H.G.M., Ribeiro, E.O., Matheson, G.S.G., Lima, J.A.M., Parente, C.E., 2009. Reconstituição do clima de ondas no sul-sudeste brasileiro entre 1997 e 2005. Revista Brasileira de Oceanografia 27 (3), 427–445 São Paulo.
Alves, J.H.G.M., Scott, S., Chawla, A., Tolman, H., van der Westhuysen, A., 2015. Operational wave guidance at the U.S. National Weather Service during Tropical/Post–Tropical Storm Sandy, October 2012. Monthly Weath. Rev. 143 (5), 1687–1702.
Alves, J.H.G.M., Chawla, A., Tolman, H.L., Schwab, D., Lang, G., Mann, G., 2014. The operational implementation of a great lakes wave forecasting system at NOAA/NCEP. Weather Forecast. 29, 1473–1497.
Alves, J.H.G.M, Campos, R.M., Guedes Soares, C., Parente, C.E., 2017. Improving surface wind databases for extreme wind-wave simulation and analysis in the south Atlantic ocean. NCEP Office Note 491, p1–38. http://dx.doi.org/10.7289/V5/ON-NCEP-491.
Amante, C., Eakins, B.W., 2009. ETOPO1 1 Arc-Minute Global Relief Model: Procedures, Data Sources and Analysis. NOAA Technical Memorandum NESDIS NGDC-24. National Geophysical Data Center, NOAA.
Appendini, C.M., Torres-Freyermutha, A., Oropeza, F., Salles, P., López, J., Mendoza, E.T., 2012. Wave modeling performance in the Gulf of Mexico and Western Caribbean: Wind reanalyses assessment. Appl. Ocean Res. 39, 20–30.
Ardhuin, F., Herbers, T.H.C., Watts, K.P, Van Vledder, G., Jensen, R., Graber, H.C., 2007a. Swell and slanting-fetch effects on wind wave growth. J. Phys. Oceanogr. 37, 908–931.
Ardhuin, F., Bertotti, L., Bidlot, J., Cavaleri, L., Filipetto, V., Lefevre, J.-M., Wittmann, P., 2007b. Comparison of wind and wave measurements and models in the Western Mediterranean Sea. Ocean Eng. 34, 526–541.
Ardhuin, F., Rogers, E., Babanin, A.V., Filipot, J.-F., Magne, R., Roland, A., van der Westhuysen, A., Queffeulou, P., Lefevre, J.-M., Aouf, L., Collard, F., 2010. Semiempirical dissipation source functions for ocean waves. Part I: Definition, calibration, and validation. J. Phys. Oceanogr. 40, 1917–1941.
Ash, E, Busswell, G, Pinnock, S, 2012. DUE Globwave wave Data Handbook. UK Ltd., Logica, pp. 74.
Babanin, A.V., Banner, M.L., Young, I.R., Donelan, M.A., 2007. Wave follower measurements of the wind input spectral function. Part 3. Parameterization of the wind input enhancement due to wave breaking. J. Phys. Oceanogr. 37 (2), 2764–2775.
Bidlot, J.-R., Janssen, P., Abdalla, P., 2007. A revised formulation of ocean wave dissipation and its model impact. ECMWF Tech. Rep. Memo 509, Reading, United Kingdom p.27.
Bidlot, J.-R., Abdalla, S., Janssen, P., 2005. A revised formulation for ocean wave dissipation in CY25R1. Research Dept. Tech. Rep. Memo. 35 R60.9/JB/0516, ECMWF, Reading, United Kingdom.
Burgers, G., Makin, K.V., 1992. Boundary-layer model results for wind-sea growth. J. Phys. Oceanogr. 23, 372–385.
Caires, S., Sterl, A., 2005. 100-Year Return Value Estimates for Ocean Wind Speed and Significant Wave Height from the ERA-40 Data. J. Climate 18, 1032–1048.
Caires, S., Sterl, A., Bidlot, J.R., Graham, N., Swail, V., 2004. Intercomparison of different wind–wave reanalyses. J. Clim. 17 (10), 1893–1913.
Campos, R.M., Guedes Soares, C., 2016a. Estimating extreme waves in brazil using regional frequency analysis. In: Proceedings of the ASME 2016 35th International Conference on Ocean, Offshore and Arctic Engineering, OMAE2016-54461, June 19-24.
Campos, R.M., Guedes Soares, C., 2016b. Comparison and assessment of three wave hindcasts in the north Atlantic ocean. J. Operational Oceanogr. 9, 26–44. http://dx.doi.org/10.1080/1755876X.2016.1200249.
Campos, R.M., Guedes Soares, C., 2016c. Comparison of HIPOCAS and ERA wind and wave reanalyses in the North Atlantic Ocean. Ocean Eng 112, 320–334.
Campos, R.M., Parente, C.E., Camargo, R., 2012. Extreme wave analysis in Campos Basin (Rio de Janeiro – Brazil) associated with extra-tropical cyclones and anticyclones. In: Proceedings of the ASME 2012 31st International Conference on Ocean, Offshore and Arctic Engineering, OMAE2012-83117, June 10-15.
Cardone, V.J., Cox, A.T., 2011. Modelling very extreme sea states (VESS) in real and synthetic design level storms. In: Proceedings of the OMAE2011 Conference. Rotterdam, The Netherlands. pp. 2011.
Cardone, V.J., Jensen, R.E., Resio, D.T., Swail, V.R., Cox, A.T., 1996. Evaluation of contemporary ocean wave models in rare events: the Halloween storm October and the storm of century of March 1993. J. Atmosph. Ocean Technol. 13, 198–230.
Cavaleri, L., 2009. Wave Modeling — Missing the Peaks. J. Phys. Oceanogr. 39, 2757–2778.
Cavaleri, L., Bertotti, L., 2006. The improvement of modeled wind and wave fields with increasing resolution. Ocean Eng 33, 553–565.
Cavaleri, L., Bertotti, L., 2004. Accuracy of the modelled wind and wave fields in enclosed seas. Tellus A 56, 167–175.
Cavaleri, L., Alves, J.H.G.M., Ardhuin, F., Babanin, A., Banner, M., Belibassakis, K., Benoit, M., Donelan, M., Groeneweg, J., Herbers, T.H.C., Hwang, P., Janssen, P.A.E.M., Janssen, T., Lavrenov, I.V., Magne, R., Monbaliu, J., Onorato, M., Polnikov, V., Resio, D., Rogers, W.E., Sheremet, A., McKee Smith, J., Tolman, H.L., Van Vledder, G., Wolf, J., Young, I., 2007. Prog. Oceanography 75, 603–674. http://dx.doi.org/10.1016/j.pocean.2007.05.005.
Chao, Y.Y., Alves, J.H.G.M., Tolman, H.L., 2005. An Operational System for Predicting Hurricane-Generated Wind Waves in the North Atlantic Ocean*. Weather Forecasting 20 (4), 652–671.
Chawla, A., Tolman, H.L., 2007. Automated Grid Generation For WAVEWATCH III. National Center for Environmental Prediction, Washington DC Technical note 254, NCEP/NOAA/NWS.
Chawla, A., Spindler, D.M., Tolman, H.L., 2013. Validation of a thirty year wave hindcast using the Climate Forecast System Reanalysis winds. Ocean Modell 70, 189–206.
Cooper, C.K., Forristall, G.Z., 1997. The use of satellite altimeter data to estimate extreme wave climate. J. Atmosph. Oceanic Technol. 14 (2), 254–266.
Dee, D.P., Uppala, S.M., Simmons, A.J., Berrisford, P., Poli, P., Kobayashi, S., Andrae, U., Balmaseda, M.A., Balsamo, G., Bauer, P., Bechtold, P., Beljaars, A.C.M., Van de Berg, L., Bidlot, J., Bormann, N., Delsol, C., Dragani, R., Fuentes, M., Geer, A.J., Haimberger, L., Healy, S.B., Hersbach, H., Hólm, E.V., Isaksen, L., Kållberg, P., Köhler, M., Matricardi, M., McNally, A.P., Monge-Sanz, B.M., Morcrette, J.-J., Park, B.-K., Peubey, C., Rosnay, P., Tavolato, C., Thépaut and, F., Vitart, J.-N., 2011. The ERA-Interim reanalysis: configuration and performance of the data assimilation system. Q. J. R. Meteorol. Soc. 137, 553–597.
Dragani, W.C., Cerne, B.S., Campetella, C.M., Possia, N.E., Campos, M.I., 2013. Synoptic patterns associated with the highest wind-waves at the mouth of the Río de la Plata estuary. Dyn. Atmosph. Oceans 61-62, 1–13.
Feng, H., Vandemark, D., Quilfen, Y., Chapron, B., Beckley, B., 2006. Assessment of wind-forcing impact on a global wind-wave model using the TOPEX altimeter. Ocean Eng. 33, 1431–1461.
Freilich, M.H., Vanhoff, B.A., 2006. The accuracy of preliminary WindSat vector wind measurements: Comparisons with NDBC buoys and QuikSCAT. IEEE Trans. Geosci. Remote Sens. 44, 622–637.
Gan, M.A., Rao, B.V., 1991. Surface ciclogenesis over South America. Mon. Wea. Rev. 119, 293–302.
Gibson, J.K., Kallberg, P., Uppala, S.A, Hernandez, A., Nomura, A., Serrano, E., 1997. ERA description. ECMWF *Re*-Anal. Proj. Rep. Series 1, 89.
GlobWave/DD/PUG. GLOBWAVE Product User Guide. A/I/P. SatOC, Ifremer, NOC,CLS, 2013, Report No.: 21891/08/I-EC.
Godoi, V.A., Parente, C.E., Torres, A.R.T, 2014. An overview of events of high sea waves at the mouth of Guanabara Bay. Pan-Am. J. Aquatic Sci. 9 (2), 70–87.
Hanna, S., Heinold, D., 1985. Development and application of a simple method for evaluating air quality. In: API Pub. No. 4409, Washington, DC, Washington, USA.
Holthuijsen, L.H., Booji, N., Bertotti, L., 1996. The propagation of wind errors through ocean wave hindcasts. J. Offshore Mech. Arct. Eng. 118, 184–189.
Innocentini, V., Caetano Neto, S., 1996. A Case Study of the 9 August 1988 South Atlantic Storm: Numerical simulations of the wave Activity. Weather Forecasting 11, 78–88.
Innocentini, V., Caetano, E., Carvalho, J.T., 2014. A procedure for operational use of wave hindcasts to identify landfall of heavy swell. Weather Forecasting 29, 349–365.
Janssen, P.A.E.M., 1991. Quasi-linear theory of wind wave generation applied to wave forecasting. J. Phys. Oceanogr. 21, 1631–1642.
Janssen, P.A.E.M., 1982. Quasilinear approximation for the spectrum of wind-generated water waves. J. Fluid Mech. 117, 493–506.
JPL, 2001. QuikSCAT science data product user's manual (version 2.0) Jet Propulsion Laboratory Publ. D-18053, Pasadena, CA, 84 pp. [Available online at http://podaac.jpl.nasa.gov/QuikSCAT.].
Kalnay, E., Kanamitsu, M., Kistler, R., Collins, W., Deaven, D., Gandin, L., Iredell, M., Saha, S., White, G., Woollen, J., Zhu, Y., Chelliah, M., Ebisuzaki, W., Higgins, W., Janowiak, J., Mo, K., Ropelewski, C., Wang, J., Leetmaa, A., Reynolds, R., Jenne, R., Joseph, D., 1996. The NCEP/NCAR reanalysis project. Bul. Am. Meteorol. Soc. 77 (3), 437–471.
Kistler, R., Kalnay, E., Collins, W., Saha, S., White, G., Woollen, J., Chelliah, M., Ebisuzaki, W., Kanamitsu, M., Kousky, V., Van den Dool, H., Jenne, R., Fiorino, M., 2001. The NCEP-NCAR 50-year reanalysis: Monthly means CD-Rom and documentation. Bull. Amer. Meteorol. Soc. 82, 247–267.
Kurihara, Y., Bender, M.A., Ross, R.J., 1993. An initialization scheme of hurricane models by vortex specification. Month. Weather Rev. 121, 2030–2045.
Liu, W.T., Katsaros, K.B., Businger, J.A., 1979. Bulk Parameterizations of Air-Sea Exchanges of Heat and Water Vapor Including Molecular Constraints at the Interface. J. Atmosph. Sci. 36, 1722–1735.
Mentaschi, L., Besio, G., Cassola, F., Mazzino, A., 2013. Problems in RMSE-based wave model validations. Ocean Model. 72, 53–58.
Murray, R.J., Simmonds, I., 1991. A numerical scheme for tracking cyclone centers from digital data. Aust. Meteor. Mag. 39, 155–166.
Nascimento, M.X., 2013. Analise das Condiçoes Meteo-Oceanograficas na Regiao da Bacia de Santos. MSc. Thesis. COPPE/UFRJ, Rio de Janeiro, RJ, Brazil.
Padilla-Hernandez, R., Perrie, W., Toulany, B., Smith, P.C., Zhang, W., Jimenez-Hernandez, S., 2004. Intercomparison of modern operational wave models. In: 8th International Workshop on Wave Hindcasting and Forecasting. North Shore, Oahu, Hawaii. November 2004.
Parente, C.E., 1999. Uma Nova Técnica Espectral para Análise Direcional de Ondas. PhD Thesis. COPPE/UFRJ, Rio de Janeiro, RJ, Brazil.
Pianca, C., Mazzini, P.L.F., Siegle, E., 2010. Brazilian Offshore Wave Climate Based on NWW3 Reanalysis. Brazilian J. Oceanogr. 58 (1), 53–70.
Pinho, U.F., 2003. Caracterização dos estados de mar na Bacia de Campos. M.*Sc*. Thesis. COPPE/UFRJ, Rio de Janeiro, RJ, Brazil.
Ponce de Leon, S., Guedes Soares, C., 2014. Extreme wave parameters under North Atlantic extratropical cyclones. Ocean Model 81, 78–88.
Ponce de Leon, S., Guedes Soares, C., 2008. Sensitivity of wave model predictions to wind fields in the Western Mediterranean sea. Coast. Eng. 55, 920–929.
Quilfen, Y., Prigent, C., Chapron, B., Mouche, A.A., Houti, N., 2007. The potential of QuikSCAT and WindSat observations for the estimation of sea surface wind vector under severe weather conditions. J. Geophys. Res. 112, C09023. http://dx.doi.org/10.1029/2007JC004163.
Reboita, M.S., 2008. Ciclones Extratropicais sobre o Atlântico Sul: Simulação Climática e Experimentos de Sensibilidade. PhD Thesis. IAG-USP, São Paulo, SP, Brazil.
Reboita, M.S., Da Rocha, R.P., Ambrizzi, T., Sugahara, S., 2009. South Atlantic Ocean Cyclogenesis Climatology Simulated by Regional Climate Model (RegCM3). Climate Dyn. http://dx.doi.org/10.1007/s00382-009-0668-7.
Rogers, W.E., Dykes, J.D., Wang, D., Carroll, S.N., Watson, K., 2012a. Validation Test Report for WAVEWATCH III. NRL Memorandum Report 7320-12-9425, 75 pp.

Rogers, W.E., Babanin, A.V., Wang, D.W., 2012b. Observation-Consistent Input and Whitecapping Dissipation in a Model for Wind-Generated Surface Waves: Description and Simple Calculations. J. Atmos. Oceanic Tech. 29 (9), 1329–1346.
Rocha, R.P., Sugahara, S., Silveira, R.B., 2004. Sea waves generated by extratropical cyclones in the South Atlantic Ocean: Hindcast and validation against altimeter data. Weather Forecast. 19, 398–410.
Romeu, M.A.R., Fontoura, J.A.S., Melo, E., 2015. Typical scenarios of wave regimes off Rio Grande do Sul, southern Brazil. J. Coastal Res. 31, 61–68. 10.2112/JCOASTRES-12-00085.1.
Saha, S., Moorthi, S., Pan, H., Wu, X., Wang, J., Nadiga, S., Tripp, P., Kistler, R., Wollen, J., Behringer, D., Liu, H., Stokes, D., Grumbine, R., Gayno, G., Wang, J., Hou, Y., Chuang, H., Juang, H., Sela, J., Iredell, M., Treadon, R., Kleist, D., VanDelst, P., Keyser, D., Derber, J., Ek, M., Meng, J., Wei, H., Yang, R., Lord, S., van den Dool, H., Kumar, A., Wang, W., Long, C., Chelliah, M., Xue, Y., Huang, B., Schemm, J., Ebisuzaki, W., Lin, R., Xie, P., Chen, M., Zhou, S., Higgins, W., Zou, C., Liu, Q., Chen, Y., Han, Y., Cucurull, L., Reynolds, R., Rutledge, G., Goldberg, M., 2010. The NCEP climate forecast system reanalysis. Bull. Am. Meteorol. Soc. 91, 1015–1057.
Stopa, J.E., Cheung, K.F., 2014. Intercomparison of wind and wave data from the ECMWF Reanalysis Interim and the NCEP Climate Forecast System Reanalysis. Ocean Modell. 75, 65–83.
Sugahara, S., 2000. Variacao Anual da Frequencia de Ciclones no Atlantico Sul. XI. In: Congresso Brasileiro de Meteorologia, II Encontro Brasileiro de Interacao Oceano-Atmosfera. Rio de Janeiro. 1. pp. 2607–2611.
Swail, V.R., Cox, A.T., 2000. On the use of NCEP-NCAR reanalysis surface marine wind fields for a long-term North Atlantic wave hindcast. J. Atmos. Oceanic Technol. 17, 532–545.
Taylor, K.E., 2001. Summarizing multiple aspects of model performance in a single diagram. J. Geophys. Res. 106, 7183–7192.
Teixeira, J.C., Abreu, M.P., Guedes Soares, C., 1995. Uncertainty of ocean wave hindcasts due to wind modelling. J. Offshore Mech. Arct. Eng. 117, 294–297.
Tolman, H.L., 1998. Validation of NCEP's ocean winds for the use in wind wave models. Global Atmos. Ocean Syst. 6 (3), 243–268.
Tolman, H.L., Alves, J.H.G.M., 2005. Numerical modeling of wind waves generated by tropical cyclones using moving grids. Ocean Modell 9, 305–323.
Tolman, H.L., Chalikov, D., 1996. Source terms in a third-generation wind wave model. J Phys Oceanogr 26, 2497–2518.
Tolman, H.L. and the WAVEWATCH III Development Group, 2014. User manual and system documentation of WAVEWATCH III version 4.18. EMC/MMAB/NCEP/NOAA, MMAB Contribution No. 316.
Uppala, S.M., Kållberg, P.W., Simmons, A.J., Andrae, U., da Costa Bechtold, V., Fiorino, M., Gibson, J.K., Haseler, J., Hernandez, A., Kelly, G.A., Li, X., Onogi, K., Saarinen, S., Sokka, N., Allan, R.P., Andersson, E., Arpe, K., Balmaseda, M.A., Beljaars, A.C.M., van de Berg, L., Bidlot, J., Bormann, N., Caires, S., Chevallier, F., Dethof, A., Dragosavac, M., Fisher, M., Fuentes, M., Hagemann, S., Hólm, E., Hoskins, B.J., Isaksen, L., Janssen, P.A.E.M., Jenne, R., McNally, A.P., Mahfouf, J.-F., Morcrette, J.-J., Rayner, N.A., Saunders, R.W., Simon, P., Sterl, A., Trenberth, K.E., Untch, A., Vasiljevic, D., Viterbo, P., Woollen, J., 2005. The ERA-40 re-analysis. Q. J. R. Meteorol Soc. 131, 2961–3012.
Van Vledder, G.Ph, Akpinar, A., 2015. Wave model predictions in the Black Sea: Sensitivity to wind fields. Appl. Ocean Res. 53, 161–178.
Vanem, E., Walker, S.E., 2013. Identifying trends in the ocean wave climate by time series analyses of significant wave height data. Ocean Eng 61, 148–160.
Wessel, P., Smith, W.H.F., 1996. A global self-consistent, hierarchical, high-resolution shoreline database. J. Geophys. Res. 101, 8741–8743 #B4.
Wu, X., Grumbine, R., 2013. Sea ice in the NCEP climate forecast system reanalysis. science and technology infusion climate bulletin. In: 38th NOAA Annual Climate Diagnostics and Prediction Workshop.
Young, I.R., Holland, G.J., 1996. Atlas of the oceans: Wind and Wave Climate. Pergamon Press, New York, pp. 241.
Zhang, H., Reynolds, R., Bates, J., 2006. Blended and gridded high resolution global sea surface wind speed and climatology from multiple satellites: 1987–present. In: Proceeding of American Meteorological Society 2006 Annual Meeting. Atlanta, GA, America, 29 January–2 February. 2. pp. 23.